

AD-A238 319



2



# High Strain Rate Characterization of Ceramics in Shear

Amos Gilat  
Department of Engineering Mechanics

DTIC  
ELECTE  
JUL 08 1991  
S D D

Department of the Navy  
Office of Naval Research  
Arlington, Virginia 22217

Contract No. N00014-88-K-0733  
Final Report

**DISTRIBUTION STATEMENT A**

Approved for public release  
Distribution Unlimited

June 1991

91-03885





# High Strain Rate Characterization of Ceramics in Shear

Amos Gilai  
Department of Engineering Mechanics

**Department of the Navy**  
Office of Naval Research  
Arlington, Virginia 22217

Contract No. N00014-88-K-0733  
Final Report  
RF Project No. 767094/721496

June 1991

## TABLE OF CONTENTS

1.	INTRODUCTION.....	3
2.	EXPERIMENTS.....	4
2.1	Experimental Technique.....	4
2.2	Specimens.....	5
2.3	Experimental Results.....	6
	2.3.1 Results from Tests on Aluminum Oxide.....	6
	2.3.2 Results from Tests on Titanium Diboride and Aluminum Nitride.....	7
3.	NUMERICAL ANALYSIS.....	7
3.1	Spool Specimens.....	8
3.2	Prism Specimens.....	8
4.	DISCUSSION.....	9
5.	CONCLUSIONS.....	14
6.	REFERENCES.....	15
7.	APPENDIX: Tests with 6061-T651 Aluminum.....	17

ACQUISITION	
NTIS GRA&I	
DTIC TAB	
Unannounced	
Justification	
By	
Date	
Dist	
A-1	

## 1. INTRODUCTION

Many ceramic materials are being used in applications that involve high rates of loading. Examples are jet engine parts and protective armor components. Most of the available data with regard to dynamic response of ceramics have been obtained from experiments that involve compressive loading. Two techniques, the normal plate impact and the compression split Hopkinson bar, are most commonly used for testing under high rate loading in compression. Results from normal plate impact tests generally show a remarkable increase in the yield stress when the Hogionot Elastic Limit (HEL) is transformed to uniaxial stress and compared with the static uniaxial yield stress. Tests on commercial alumina (AD-85) by Rosenberg and Yeshurun (1985), for example, show a dynamic yield strength of 43 Kbars compared to a quasi-static yield strength of 19.3 Kbars. High strain rate tests with the compression split Hopkinson bar have been conducted by Lankford (1981). His results from tests on aluminum oxide at various temperatures show an increase in the compressive strength with increasing strain rate.

In addition to characterization in the normal direction, the plate impact experiment provides some indirect data with regard to the shear strength of ceramics. Within the elastic limit at stress levels up to the HEL, the magnitude of the shear stress can be determined directly by theory of elasticity. Tests on AL-995 alumina by Ahrens et al. (1968), for example, show shear stress (at the HEL) of 52 Kbar which is at least one order of magnitude higher than the stress in quasi-static tests. Above the HEL the existence of shear strength can be determined if an offset exists between the measured Hogionot curve and the Hydrostatic curve. Experimental results show that some materials lose their shear resistance immediately or gradually above the HEL (Graham and Brooks (1971), Gust and Royce (1971), Bless and Ahrens (1976), and Grady et al. (1975)). The loss of shear strength during normal impact is also observed in tests on quartz which has zero piezoelectric response when no shear stress component exists (Graham and Brooks (1971)). Although the shear behavior of ceramics appears to be affected by the rate of loading, the only data available from tests at high deformation rate are from plate impact experiments in which the hydrostatic component of the stress dominates and may affect the shear response.

The objective of the present research is to study the response of ceramics that can potentially be used as armor materials under dynamic loading in shear. Experiments have been conducted using the torsional split Hopkinson bar technique. This technique is commonly used for testing ductile materials and the present application to very brittle materials is examined carefully.

Tests have been conducted with hot pressed aluminum oxide and titanium diboride, both made by Cercom Inc., and with aluminum nitride supplied by Dow Chemical. Most of the tests were done with spool-shaped specimens which is the standard geometry used for testing ductile materials in the torsional split Hopkinson bar apparatus. These specimens were machined from thick plates. In addition, a method was developed for testing small prism-shaped specimens. This was done in an effort to develop a screening test for newly-developed materials in which specimens will be machined from thin plates. Pilot tests have been conducted with prism shaped specimens made of aluminum oxide.

The experiments have been modeled with a three-dimensional elastic finite element analysis. Since the materials are very brittle, correlation can be made between the initial elastic response measured in the tests and the calculated stress distribution.

The results provide a strong indication of strain rate sensitivity. The stresses in the specimens when initial fracture occurs appear to be significantly higher than the stresses observed in low rate testing. This conclusion, however, is presently inconclusive since it is obtained from comparison with quasi-static data obtained in tests with different type of loading.

## 2. EXPERIMENTS

### 2.1 Experimental Technique

The torsional split Hopkinson bar technique has been used for the testing. In this technique a short material specimen is placed between two bars. The specimen is loaded by a torsional wave that is generated in one of the bars (input bar). Upon loading, part of the wave is transmitted through the specimen to the

other bar (output bar) and part is reflected back to the input bar. The history of the load and deformation in the specimen is determined by monitoring the stress waves in the bars which remain elastic during the test. The technique has been introduced with compression loading by Kolsky (1949). A detailed description of the torsional version is given by Hartley, Duffy, and Hawley (1985). A schematic description of the apparatus used for the present research is shown in Fig. 2.1.

## 2.2 Specimens

Specimens having two different geometries have been used in the tests. One is a thin-walled tube that is obtained by machining a short section of a thick-walled tube. This specimen, known as a spool-shaped specimen, is shown in Fig. 2.2. The specimen proper is the short thin-walled section in the middle. This geometry has successfully been used in the past for testing ductile materials. Experiments and numerical simulations have shown that the stresses and strains in the specimen during plastic deformation are nearly homogeneous. The corner at the edge of the specimen appears to have no significant effect. The situation is different when brittle materials are tested. Such materials may fracture prematurely at the corner due to the stress concentration. Since the ceramics studied in the present research are very brittle, the effect of the corner on the measurements is carefully examined. Tests on one of the materials (aluminum oxide) were conducted with spool-shaped specimens of different dimensions. This was accompanied by three-dimensional elastic finite element analysis.

The second type of specimens used in the tests are prism-shaped specimens. Two different geometries (A and B), shown in Fig 2.3, were used. The specimen proper is the reduced middle section of the prism. In each test two prisms are placed into holders as shown in Fig. 2.4. A small gap exists between the two faces of the holders. The specimen proper is positioned across that gap. The assembly is cemented to the bars of the split Hopkinson apparatus. In specimens of type B the specimen proper has the same dimensions as in type A while the flanges are wider. The prism specimens of type B have been introduced following the testing of specimens of type A. Details are discussed in section 4. Three-dimensional finite element analysis is used for determining the stress distribution in the specimen and relating it to the torque measured on the bars.

The prism-shaped specimens are introduced in an effort to use a specimen made of ceramic material with an easy geometry to machine from thin plates. An objective of the research is to make a correlation between the strength measured with spool and prism specimens. Once this is achieved the prism-shaped specimens, which are far less expensive to make than spool specimens, could be used for screening tests of newly-developed ceramics.

## 2.3 Experimental Results

A summary of the experiments conducted is given in Table 2.1(page 16). Experiments with spool-shaped specimens have been conducted with aluminum oxide, titanium diboride, and aluminum nitride. Experiments with prism-shaped specimens have been done only with aluminum oxide. The aluminum oxide is hot pressed Ebon A made by Cercom Inc. The titanium diboride was also purchased from Cercom and the aluminum nitride was obtained from Dow Chemical. In addition to tests with ceramics, several tests have been conducted with 6061-T651 aluminum using spool-shaped and prism-shaped specimens. The objective of these tests is to examine the relationship between the results obtained with the two specimen geometries using a material whose response is known. The results from these tests are described in the Appendix.

An example of raw data measured during a test on the split Hopkinson bar apparatus is shown in Figure 2.5. The figure shows the recorded wave profiles at the three strain gage locations from test number 89-10. The history of the strain rate in the specimen, obtained by manipulating the recorded signals is shown in Fig. 2.6. The stress-strain diagram for this test is included in Fig. 2.7. The strain is obtained by integrating the strain rate. The stress is determined from the gages on the output bar assuming homogeneous stress distribution in the specimen's wall. The wave profiles shown in Fig. 2.5 are original raw data recorded by digital 4094C Nicolet Oscilloscope. All the experimental curves are obtained by manipulating the recorded raw data. None of the diagrams shown in this report have been "smoothed" or averaged electronically or numerically.

### 2.3.1 Results from Tests on Aluminum Oxide (Ebon A)

The hot pressed aluminum oxide (Ebon A made by Cercom Inc.) was the most extensively tested material in the present research. This material was also chosen as the "model" ceramic material for examining the correlation between

tests with spool-shaped specimens of different dimensions and between the spool shaped and prism-shaped specimens. The results from the tests with the spool geometry are shown in Figs. 2.7 and 2.8. Each figure shows results from three tests of spool specimens having the same dimensions. Two different sets of dimensions are used in order to have two different stress concentrations at the corner between the specimen proper and the flange.

Results from tests with prism-shaped specimens are shown in Figs. 2.9 - 2.11. The stress in these figures is obtained by assuming uniform stress distribution on the cross-sectional area of the specimen. In the first two tests (Fig. 2.9) both sides of the prisms were connected mechanically to the holders with two press screws on each side. The assembly was then cemented to the bars. As shown in Fig. 2.9 the results obtained from these tests are not completely consistent with each other. This is probably due to initial stresses that are introduced when the prisms are tightened to the holders. It is practically impossible to machine the notches for the prisms in the holders such that the two prisms will be perfectly aligned. To overcome this problem the prisms in the next two tests (Fig. 2.10) were first connected mechanically to a holder on one side, and then glued to the holder on the other side. This procedure ensures that there are no initial stresses in the gage section of the specimen. The results from tests with specimens connected by this method (Figs. 2.10, 2.11) show excellent reproducibility of the results.

### 2.3.2 Results from Tests on Titanium Diboride and Aluminum Nitride

The titanium diboride was purchased from Cercom Inc. and the Aluminum Nitride was obtained from Dow Chemical. Tests were conducted only with spool-shaped specimens. The dimensions are given in Table 2.1. Stress strain curves obtained in the tests are shown in Figs. 2.12 and 2.13 for the titanium diboride and aluminum nitride, respectively.

## 3. NUMERICAL ANALYSIS

The experiments have been modeled numerically using a three-dimensional elastic finite element analysis. The ABAQUS code was used and the computations carried out on the Ohio State Cray Y-MP3 supercomputer.



The most common element type used in the analysis is the C3D8 element type which in the ABAQUS source code refers to the 8-noded brick element with 2 integration points per axis. The choice of this element type has been made because it offers sufficient accuracy and is relatively computationally inexpensive as compared to other element types. The C3D6 or the 6-noded wedge element has been utilized, as and when necessary, mainly for mesh refinement and in those zones where the use of a C3D8 would have resulted in element distortion.

### 3.1 Spool Specimens

The analysis of the spool specimens was done using three-dimensional elements since two-dimensional axisymmetric elements are presently not available in the ABAQUS package. Figure 3.1 shows the specimen's section considered in the numerical analysis and the boundary conditions on this section. The discretization scheme is shown in Fig. 3.2.

The shear stress distribution on the outer rim of the specimen along the specimen length is shown in Fig. 3.3 for the spool specimens used in the tests on aluminum oxide. The stress in these figures is normalized with respect to the average shear stress. The maximum shear stress at the corner of the specimen edge and the flange is 1.74 and 1.59 times the average stress for the two specimens, respectively. As expected, the stress concentration is higher when the thickness of the flange is larger.

### 3.2 Prism Specimens

The two different geometries (A and B) of prism-shaped specimens were analyzed numerically. Figures 3.4 and 3.5 show the two geometries and the section (one-eighth of the body) in each geometry that was used for the finite element analysis. Only a section of the body is analyzed because of the symmetry relative to the x-y plane and the anti-symmetry about the other two perpendicular planes. The analysis assumes that the flanges at the two sides of the specimen proper are displaced relative to each other. This means that there is a perfect connection between the prisms and the holders and that the holders are rigid. In addition, the relative circular motion between the two sides is neglected. The boundary conditions on the sections modeled numerically are shown in Figs. 3.6 and 3.7. The finite element discretization is shown in Figs. 3.8 and 3.9.

The results from the finite element analysis are shown by the stress distribution on the middle and top planes of the specimen section (shown in Figs 3.6-3.7). For a specimen with geometry A the distribution of stresses  $\tau_{xy}$ ,  $\sigma_{xx}$ ,  $\sigma_{yy}$ , and  $\sigma_{zz}$  on the middle plane are shown in Figs. 3.10-3.13, respectively. The distribution of  $\tau_{xy}$ ,  $\sigma_{xx}$ , and  $\sigma_{yy}$  on the top plane are shown in Figs. 3.14-3.16, respectively. The stress in Figs. 3.10-3.16 is normalized with respect to the average shear stress in the cross sectional area of the specimen proper. As expected, the calculations show a strong stress concentration at the corner near the free edge of the specimen.

The distribution of the various stresses on the middle and top planes for specimens with geometry B is shown in Figs. 3.17-3.23.

#### 4. DISCUSSION

The experimental results show that data produced (stress-strain curves) in tests with identical configuration are very consistent. There is only a very small scatter in the data. This is of great significance especially in testing ceramics. The consistency of the data indicates that each batch of specimens has a homogeneous microstructure and that the machining of the specimens is uniform and has not introduced uneven surface damage. It also indicates that identical loading conditions are applied in each test.

Most of the tests have been conducted with spool-shaped specimens. The stress-strain curves from these tests Figs. 2.7, 2.8, and 2.12 have a similar appearance. There is an initial elastic response in which the stress increases linearly from zero until it reaches a well-defined maximum. Following this maximum the stress reduces rapidly to some lower level at which it stays for sometime before reducing to zero. Recovered specimens, shown in Fig. 4.1, show a brittle fracture on planes at  $45^{\circ}$  relative to the direction of the shear. This is the direction of the maximum normal stress. The fracture appears to be distributed uniformly around the circumference. The fact that the load does not reduce to zero immediately following the maximum indicates that the two sides of the specimen do not separate upon initial fracture. The tensile fracture at  $45^{\circ}$  allows

ligaments that bridge across the specimen to remain and carry load for sometime. The level of this load is approximately the same for each group of specimens. It is probably related to the details of the fracturing process such as density of initial fracture sites, friction between fractured pieces, and other details.

It should be emphasized that in Figs. 2.7, 2.8, and 2.12 the stress is obtained by assuming uniform stress distribution in the specimen's wall and the strain is determined from the relative rotation of the specimen's ends by assuming homogeneous deformation along the specimen's length. Obviously, these assumptions are not valid after the initial fracture takes place (the section of the stress strain curve following the point of maximum stress) as the fractured specimen continues to carry some load. Consequently, the stresses and strains in the curves of Figs. 2.7, 2.8, and 2.12 in sections beyond the maximum stress are not accurate. They rather represent load (torque) carried by the fractured specimen and relative rotation of the specimen's ends.

The initial section of the stress-strain curves of the spool-shaped specimens corresponds to the elastic response and, thus, can be correlated to the finite element analysis. The stress distribution along the specimen proper obtained in the numerical analysis is shown in Fig. 3.3. The stress at the middle section of the specimen is nearly equal to the stress obtained by assuming uniform stress distribution in the specimen's thin-walled cross-sectional area. At the specimen's end at the corner with the flange there is a concentration of shear stress. The stress state at the corner is still nearly a pure shear which corresponds to maximum tension on planes at  $45^{\circ}$ . From the recovered specimens it is impossible to observe the location along the specimen where fracture initiates when stress is maximum on the stress-strain curves. If it is assumed, however, that fracture initiates at the point of the highest stress at the corner, then the value of the maximum shear stress in the stress-strain diagram multiplied by the stress concentration factor gives the normal tensile stress at the instant when fracture starts.

For the spool-shaped specimen the stress concentration factor depends on the specimen's dimensions. For the aluminum oxide two groups of specimens of different dimensions have been tested with results shown in Figs. 2.7 and 2.8.

The corresponding stress concentrations for the two specimens' geometries are 1.74 and 1.59. The maximum stress in Fig. 2.7 is 251.7 MPa (average of three tests). Multiplying this value by 1.74 gives a stress of 438 MPa. For the tests in Fig. 2.8 the average maximum stress is 232.3 MPa and multiplied by the stress concentration 369 MPa. Ideally, if the maximum normal stress is the correct fracture criterion, the same value of stress should be obtained from both groups of specimens after multiplying by the stress concentrations factor. The two sets of specimens were ordered separately at different times from Cercom Inc. A check with the company revealed that the specimens in the two orders were machined from different blocks. In the second order (tests in Fig. 2.8) the specimens were machined from a 2 in. thick plate compared to a 1 in. plate in the first order (tests in Fig. 2.7). The thicker plates have a lower strength which can account for the difference obtained in the experiments.

The results from the tests on titanium diboride (Fig. 2.12) show a maximum average shear stress of 188.8 MPa. Multiplying this value by a stress concentration of 1.63 gives maximum stress of 308 MPa.

Two tests have been conducted with spool-shaped specimens made of aluminum nitride. A block made of this material was obtained from Dow Chemical. The specimens were machined by Cercom Inc. The results from the tests, Fig. 2.13, show an extremely low stress. It was very difficult to machine the specimens since the material was very brittle. It is assumed here that the block from which the specimens were made was defective or that significant damage was introduced during the machining.

Tests with prism-shaped specimens have been conducted only with specimens made of aluminum oxide. Tests have been conducted with specimens of type A and B. The stress-strain curves from these tests, Figs. 2.10 and 2.11, show an initial elastic response up to a stress of 100 MPa. At this point the slope of the diagram changes (lowers) and the stress increases further nearly linearly with strain to approximately 200 MPa. The stress and strain in Figs. 2.10 and 2.11 are obtained from the measurements on the Hopkinson bars by assuming uniform stress and strains in the cross-sectional area of the prism.

For both types of prisms the initial part of the stress-strain diagram which corresponds to an elastic response until initial fracture occurs at 100 MPa, can be correlated to the results from finite element analysis. The calculations show, Figs. 3.10 to 3.23, that the stress distribution is relatively homogeneous throughout the specimen except for a very strong localized stress concentration near the corner. At that point there is a three-dimensional state of stress that includes normal tensile stresses in addition to shear.

The fracture of the corner (when the average stress is 100MPa) reduces the stress concentration at that region and the total load that the specimen carries continues to increase. This corresponds to the section of the stress strain diagram from 100 MPa to 200 MPa. Above 200 MPa fracture progresses through the specimen which subsequently leads to total failure.

Ideally, if the stresses calculated by the elastic finite element analysis are the actual stresses in the specimens during the experiments, and if the maximum normal stress can be used as a fracture criterion for the ceramics, then the tensile stress corresponds to the initial fracture obtained in different testing configurations and specimen geometries should be the same. Comparison between the results from the tests show that the tensile stress corresponds to the initial fracture in the prism-shaped specimens is 920 MPa for type A, and 630 MPa for type B. These values should be compared with 438 MPa and 369 MPa that was obtained in the tests with the spool-shaped specimens.

The tests with the prism-shaped specimens of type A were conducted first and examination of the numerical analysis showed that the magnitude of the stress concentration is very sensitive to the imposed boundary conditions. As shown in Fig. 3.6 it is assumed in the numerical analysis that the side faces of the flange up to the corner of the specimen proper are fixed while the side of the specimen proper is free. This also implies that the adapter in which the specimen is placed is rigid. The calculations according to these boundary conditions give a stress concentration that is higher than the actual one in the experiment since, in reality, it is impossible to support the flange exactly where the specimen proper starts. Also, the adapters are not rigid as the boundary conditions imply.

Based on these observations type B specimen was designed such that the specimen proper is away from the sides of the flanges. This makes the stresses at the specimen proper less sensitive to the positioning of the flanges in the holders. As expected, the maximum tensile stress when fracture initiates is lower in type B specimens than in type A. The value, however, is still much higher than the maximum tensile stress obtained from the tests with the spool-shaped specimens.

It should be emphasized that the various specimen geometries are compared through the maximum tensile stress at initial fracture. At that instant the other principal stress in the spool specimens is compression (of the same magnitude as the tension) while in the prism specimens the other principal stresses are tension. The different states of stress definitely affect the brittle fracture and can account for at least part of the difference in the tensile stresses obtained in the spool and prism specimens.

The results indicate that a more complicated failure criterion is needed to properly predict the fracture. Hopefully, the data generated in the present research will be useful for this purpose.

At the present time no tests have been conducted at quasi-static loading rates using the same method of loading and specimens from the same batch as in the dynamic tests. Consequently, it is impossible to, directly, determine whether the ceramics tested dynamically are sensitive to the loading rate. Information obtained from Cercom Inc. shows that the maximum tensile strength, obtained from bending tests, in quasi-static loading is 200 MPa for the aluminum oxide Ebon A, and 138 MPa for the titanium diboride. These values are lower than the maximum stresses obtained in the dynamic tests with the spool-shaped specimens even when the stress concentration is not accounted for. The average stress in the spool-shaped specimens can be considered as a lower bound for the maximum stress. These results indicate that there may be a significant strain rate effect.

## 5. CONCLUSIONS

The torsional split Hopkinson bar technique can be used to study the dynamic response of ceramics. Excellent reproducibility of data is obtained in tests having identical configuration. Since ceramics are very brittle, the instant of initial fracture in the specimens is clearly noticeable in the records. Up to the initial fracture the specimens appear to undergo elastic deformation that can be modeled numerically. Consequently, if a valid fracture criterion is known, the fracture of specimens made of the same material but having different geometries could be predicted. For aluminum oxide (Ebon A), the results from testing specimens with different geometries show that their fracture can not be correlated using the maximum normal stress as a fracture criterion. A more advanced fracture criterion that will better account for the different states of stress in the various specimens is needed .

Regardless of an accurate modeling, (using average stresses as lower bounds) results from tests with aluminum oxide and titanium diboride indicate that there may be a significant strain rate effect. This conclusion is obtained from comparison with results from bending tests at quasi-static rates. Low strain rate tests with identical loading configuration as in the dynamic tests will soon be conducted. This will provide a more conclusive conclusion with regard to the effect of the loading rate.

## 6. REFERENCES

- Ahrens, T.J., Gust, W.H., and Boyce, E.B., (1968), J. Appl. Phys., 39, 4610.
- Bless, S.J. and Ahrens, T.J. (1976), J. Geophys. Res, 81, 1935.
- Grady, D.E., Murri, W.J., DeGarli, P.S., (1975), J. Geophys. Res., 80, 4857.
- Graham, R.A. and Brooks, W.P., (1971), J. Phys. Chem. Solids, 32, 2311.
- Green, A.P., (1954), J. Mech. Phys. Solids, 2, 197.
- Gust, W.H. and Royce, E.B., (1971), J. Appl. Phys., 42, 274.
- Hartley, K.A., Duffy, J., and Hawley, R.H., (1985), Metals Handbook 9th Ed. Am. Soc. Metals, 8, 218.
- Kolsky, H., (1949), Proc. Phys. Soc., London, 62B, 676.
- Lankford, J. (1981), J. Mat. Sci., 16, 1567.
- Rosenberg, Z. and Yeshurun, Y., (1985), J. Appl. Phys., 58, 3077.



TABLE 2.1: SUMMARY OF EXPERIMENTS

EXP. NO.	MATERIAL	SPECIMEN GEOMETRY	$d_o$ (in)	$d_i$ ( $d_o$ and $d_i$ are (in) shown in Fig. 2.2)
89-10	Al. Oxide	spool	0.675	0.335
89-11	Al. Oxide	spool	0.675	0.335
89-12	Al. Oxide	prism type A	dimensions shown in Fig. 2.3	
89-13	Al. Oxide	prism type A	dimensions shown in Fig. 2.3	
89-14	Al. Oxide	spool	0.675	0.335
89-16	Al. Oxide	prism type A	dimensions shown in Fig. 2.3	
89-18	Al. Oxide	prism type A	dimensions shown in Fig. 2.3	
90-1	Al. Oxide	spool	0.703	0.473
90-2	Al. Oxide	spool	0.703	0.473
90-3	Ti Diboride	spool	0.635	0.334
90-4	Ti Diboride	spool	0.635	0.334
90-5	Al. Oxide	spool	0.703	0.473
90-6	Ti. Diboride	spool	0.635	0.334
90-7	Al. Nitride	spool	0.709	0.334
90-8	Al. Nitride	spool	0.709	0.334
91-1	Al. Oxide	prism type B	dimensions shown in Fig. 2.3	
91-2	Al. Oxide	prism type B	dimensions shown in Fig. 2.3	



---

## Appendix

## APPENDIX: Tests with 6061-T651 Aluminum

In order to examine the testing procedures experiments have been conducted using the same configuration as used with the spool- and prism- shaped specimens (type A only) with specimens made of 6061-T651 aluminum. This material is a good "model" material since it is strain rate insensitive in the range of strain rates considered here and also exhibits very little strain hardening. Shear stress-strain curves from typical tests are shown in Fig. A.1. The data were processed in the same way as in the tests with ceramics. The results from tests with the spool-shaped specimens agree well with published data for this material.

The initial part of the stress-strain curve from the test with the prism-shaped specimens increases from zero more gradually than the curve from the test with the spool specimen. The stress in the stress strain curves is obtained from measuring the wave that is transmitted through the specimen. When prisms are used the motion is transmitted to the output bar through two points. This slows down the rate at which the bar accelerates during abrupt changes in the wave profiles compare to the case where spool specimen is used. It takes a finite time to set in motion the entire cross sectional area when the motion is imposed only at two points. The yielding region in the stress strain curves from tests with prisms is more rounded than in curves from tests with spools. This is due to the ductile response of the aluminum. The prism specimens yield gradually starting at the points with high stress concentration.

At large strains where the stress strain curve is nearly horizontal the stress in tests with the prisms is approximately 15% lower than the stress in tests with spool specimens. This result can be compared with theoretical analysis of Green (1954). The analysis uses slip line theory to model the deformation of a body having the geometry of the prism-shaped specimens. The theory shows that for the dimensions of prisms used in the experiments the average stress (which is the stress of the stress-strain curve) is 15.4% lower than the actual stress assuming plane stress (12.4% for plane strain). This agrees exceptionally well with the experimental results.

## FIGURE CAPTIONS

- Fig. 2.1 Schematic of the torsional split Hopkinson bar apparatus.
- Fig. 2.2 Spool-shaped specimen.
- Fig. 2.3 Prism-shaped specimens.
- Fig. 2.4 Prism shaped specimen's assembly.
- Fig. 2.5 Wave profiles recorded at the three gage locations shown in Fig. 2.1 (test 89-10).
- Fig. 2.6 Strain rate history in test number 89-10.
- Fig. 2.7 Shear stress-strain diagrams for aluminum oxide from tests with spool-shaped specimens.
- Fig. 2.8 Shear stress-strain diagrams for aluminum oxide from tests with spool-shaped specimens.
- Fig. 2.9 Shear stress-strain diagrams for aluminum oxide from tests with prism-shaped specimens of type A. Prisms connected mechanically on both sides.
- Fig. 2.10 Shear stress-strain diagrams for aluminum oxide from tests with prism-shaped specimens of type A. Prisms connected mechanically on one side and cemented on the other side.
- Fig. 2.11 Shear stress-strain diagrams for aluminum oxide from tests with prism-shaped specimens of type B. Prisms connected mechanically on one side and cemented on the other side.
- Fig. 2.12 Shear stress-strain diagram for titanium diboride.
- Fig. 2.13 Shear stress-strain diagram for aluminum nitride.
- Fig. 3.1 Spool specimen geometry and boundary conditions for the finite element analysis.
- Fig. 3.2 Finite element discretization scheme for spool specimens.
- Fig. 3.3 Shear stress distribution along the specimen.
- Fig. 3.4 Prism-shaped specimen modeled numerically (geometry A).
- Fig. 3.5 Prism-shaped specimen modeled numerically (geometry B).
- Fig. 3.6 Boundary conditions for the numerical analysis (prism A)
- Fig. 3.7 Boundary conditions for the numerical analysis (prism B)
- Fig. 3.8 Finite element discretization for prism-shaped specimens (geometry A)
- Fig. 3.9 Finite element discretization for prism-shaped specimens (geometry B).
- Fig. 3.10 Shear stress ( $\tau_{xy}$ ) distribution on the middle plane of prism specimens (geometry A)

- Fig. 3.11 Shear stress ( $\sigma_{xx}$ ) distribution on the middle plane of prism specimens  
(geometry A)
- Fig. 3.12 Shear stress ( $\sigma_{yy}$ ) distribution on the middle plane of prism specimens  
(geometry A)
- Fig. 3.13 Shear stress ( $\sigma_{zz}$ ) distribution on the middle plane of prism specimens  
(geometry A)
- Fig. 3.14 Shear stress ( $\tau_{xy}$ ) distribution on the top plane of prism specimens  
(geometry A)
- Fig. 3.15 Shear stress ( $\sigma_{xx}$ ) distribution on the top plane of prism specimens  
(geometry A)
- Fig. 3.16 Shear stress ( $\sigma_{yy}$ ) distribution on the top plane of prism specimens  
(geometry A)
- Fig. 3.17 Shear stress ( $\tau_{xy}$ ) distribution on the middle plane of prism specimens  
(geometry B)
- Fig. 3.18 Shear stress ( $\sigma_{xx}$ ) distribution on the middle plane of prism specimens  
(geometry B)
- Fig. 3.19 Shear stress ( $\sigma_{yy}$ ) distribution on the middle plane of prism specimens  
(geometry B)
- Fig. 3.20 Shear stress ( $\sigma_{zz}$ ) distribution on the middle plane of prism specimens  
(geometry B)
- Fig. 3.21 Shear stress ( $\tau_{xy}$ ) distribution on the top plane of prism specimens  
(geometry B)
- Fig. 3.22 Shear stress ( $\sigma_{xx}$ ) distribution on the top plane of prism specimens  
(geometry B)
- Fig. 3.23 Shear stress ( $\sigma_{yy}$ ) distribution on the top plane of prism specimens  
(geometry B)
- Fig. 4.1 Recovered spool-shaped aluminum oxide specimen.
- Fig. A.1 Shear stress-strain diagrams for 6061-T651 aluminum.

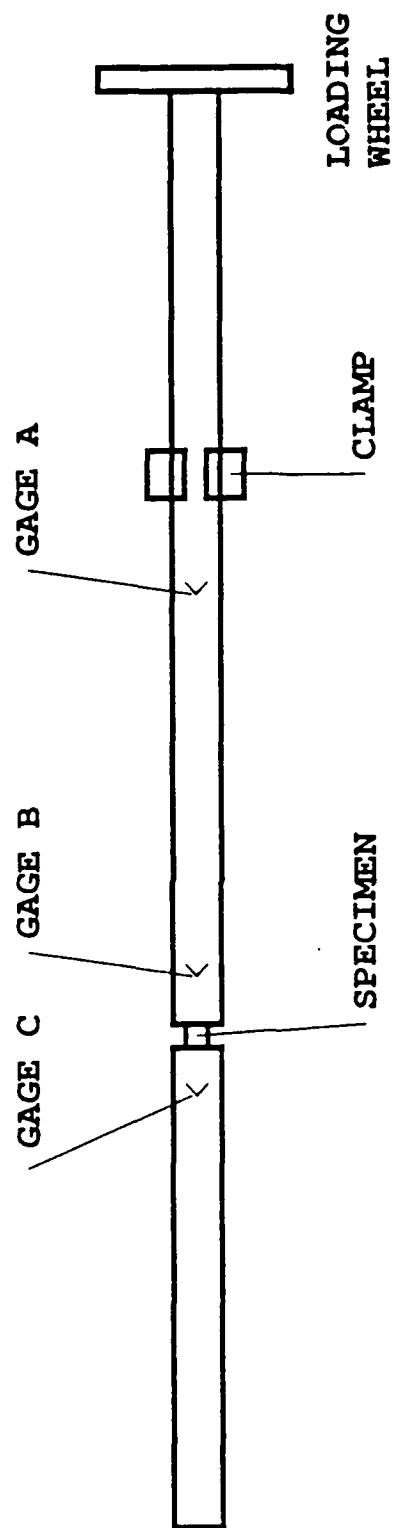
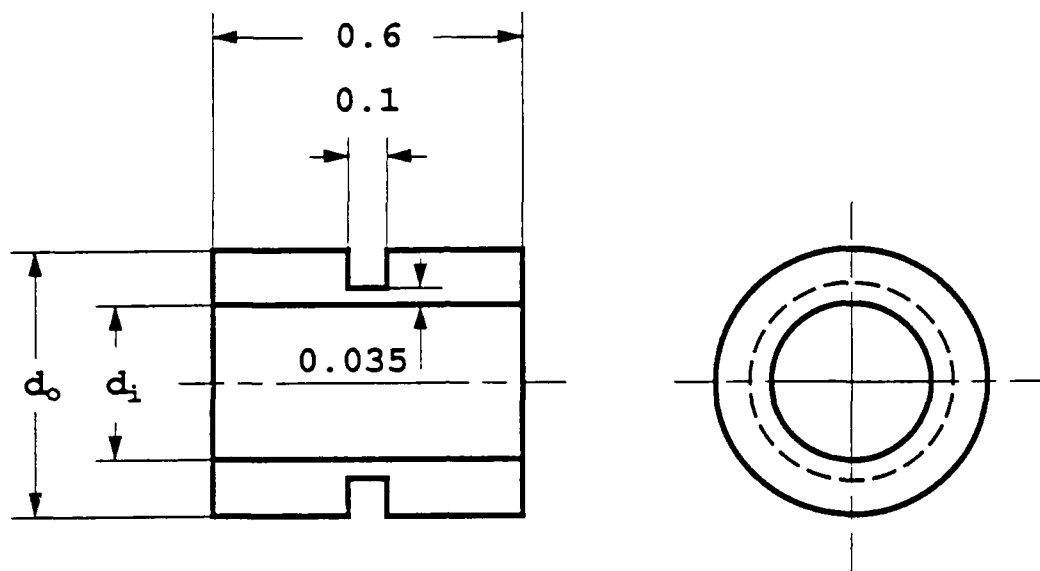
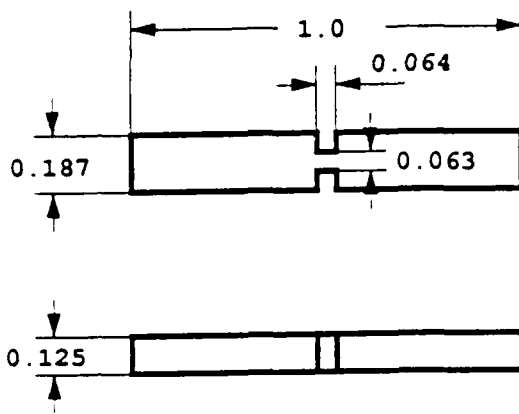


Fig. 2.1 Schematic of the torsional split Hopkinson bar apparatus.

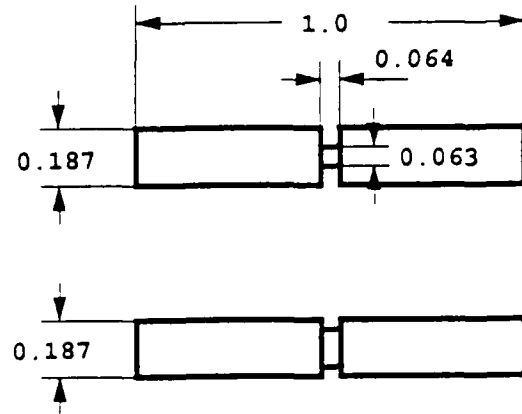


(DIMENSIONS IN INCHES)

Fig. 2.2 Spool-shaped specimen



PRISM TYPE A



PRISM TYPE B

(DIMENSIONS IN INCHES)

Fig. 2.3 Prism-shaped specimens



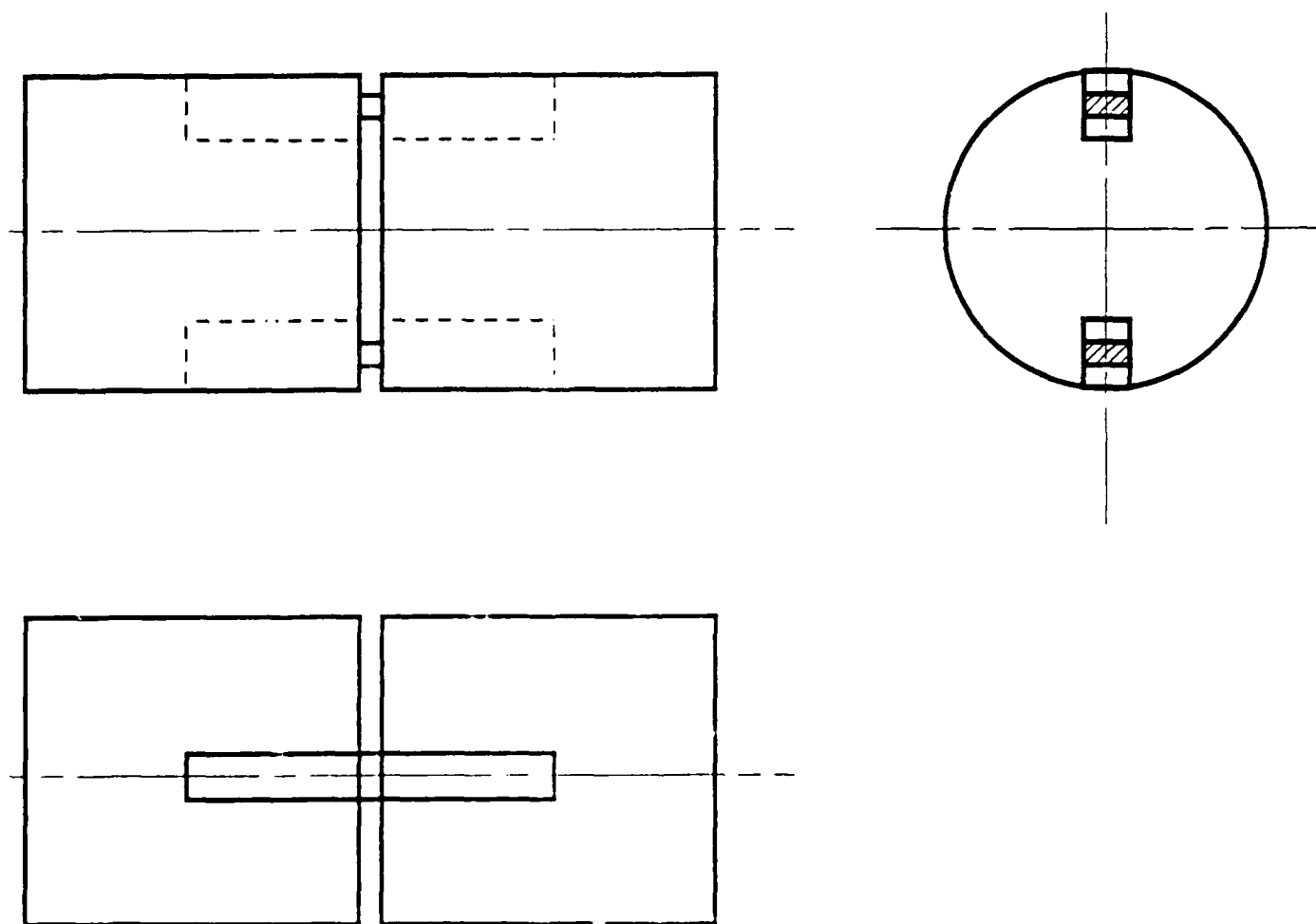


Fig. 2.4 Prism shaped specimen's assembly.

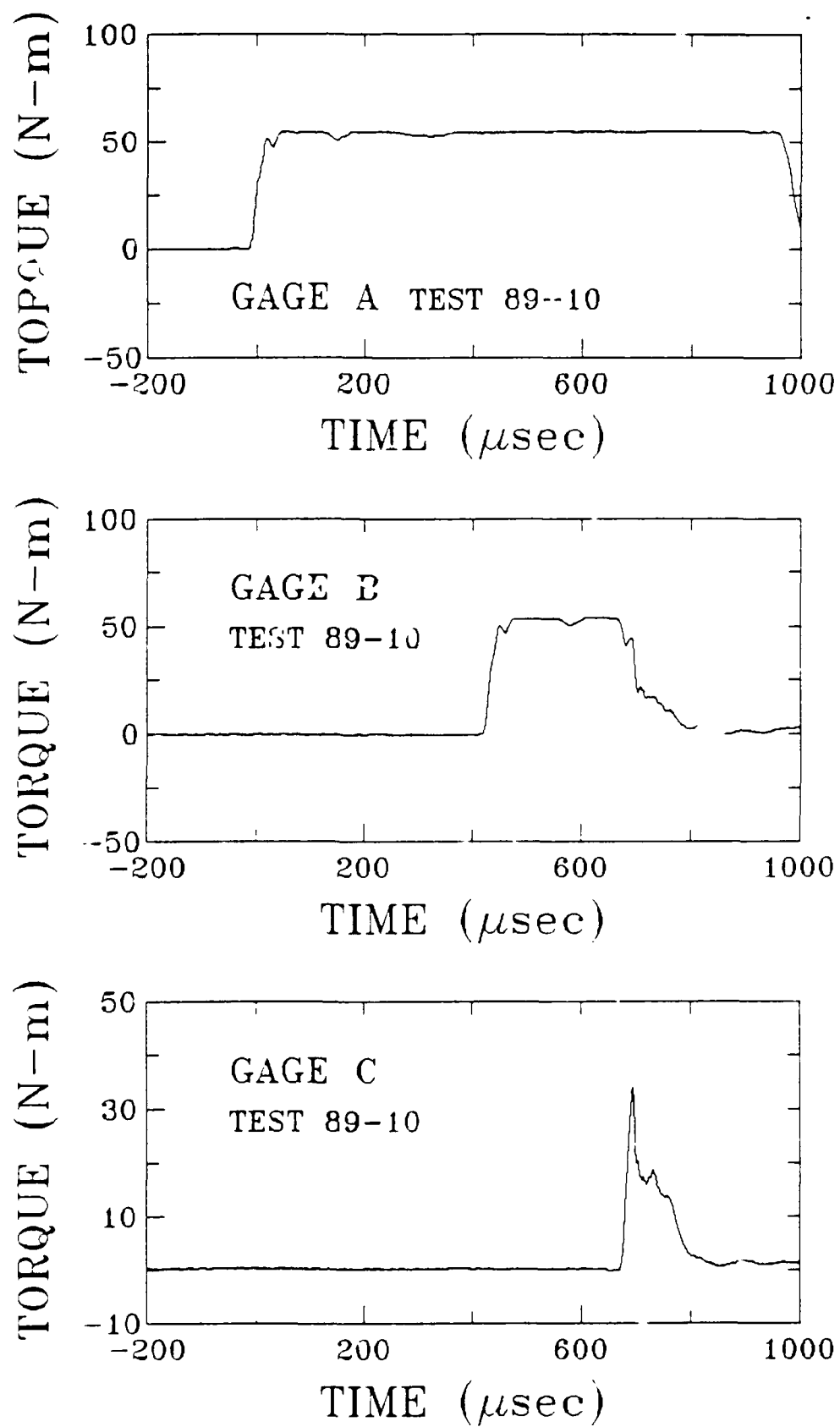


Fig. 2.5 Wave profiles recorded at the three gage locations shown in Fig. 2.1 (test 89-10).

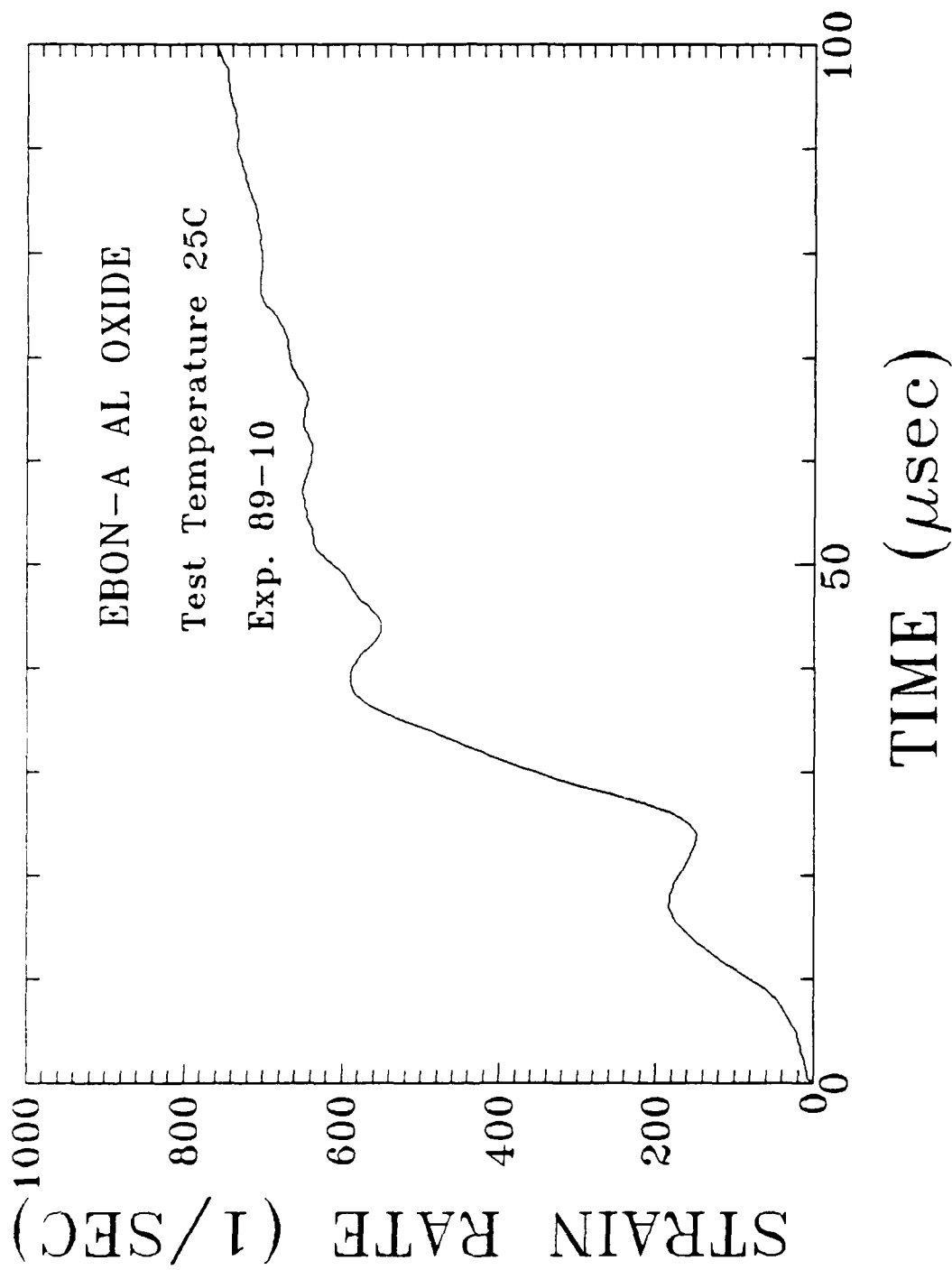


Fig. 2.6 Strain rate history in test number 89-10.

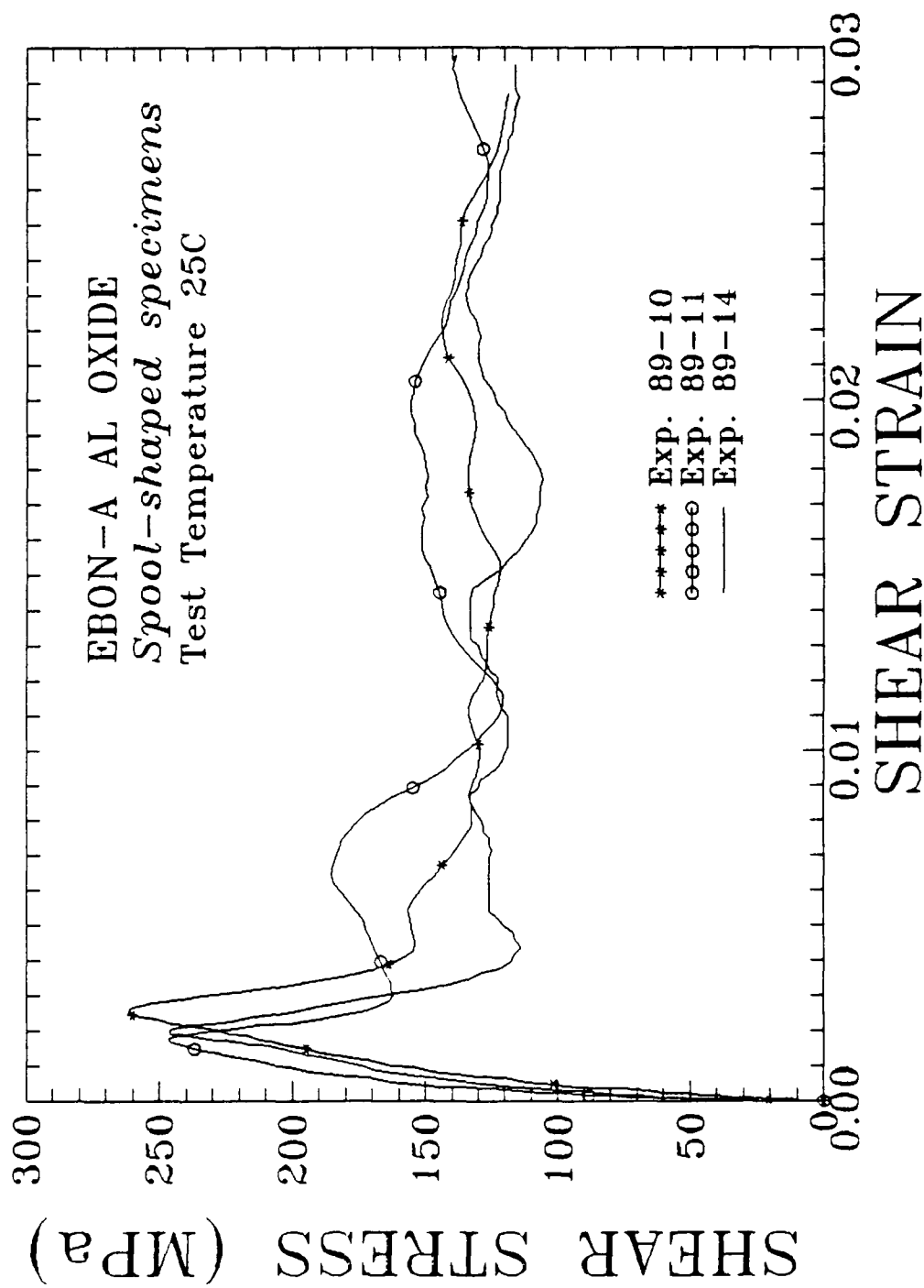


Fig. 2.7 Shear stress-strain diagrams for aluminum oxide from tests with spool-shaped specimens.

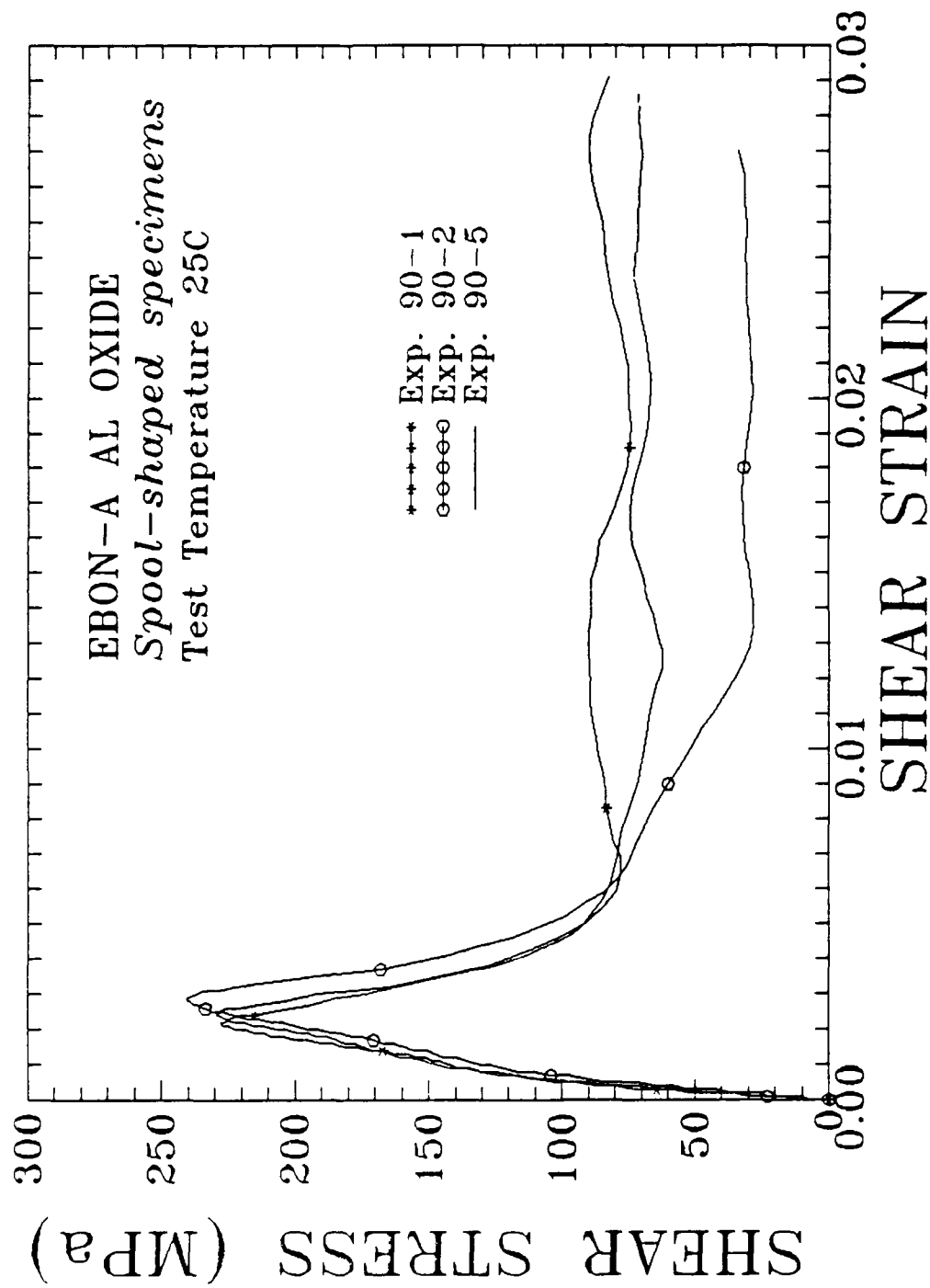


Fig. 2.8 Shear stress-strain diagrams for aluminum oxide from tests with spool-shaped specimens.

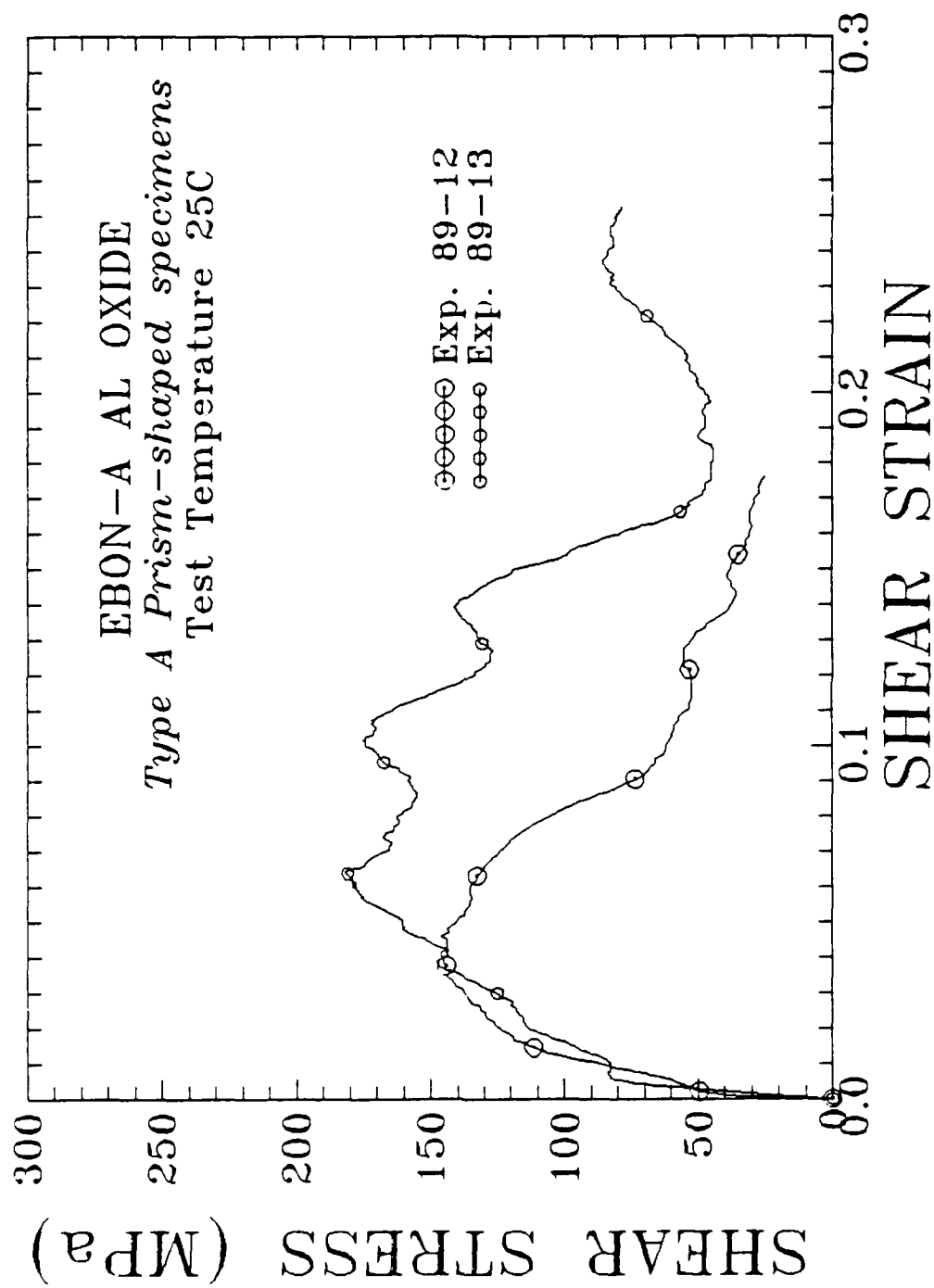


Fig. 2.9 Shear stress-strain diagrams for aluminum oxide from tests with prism-shaped specimens of type A. Prisms connected mechanically on both sides.

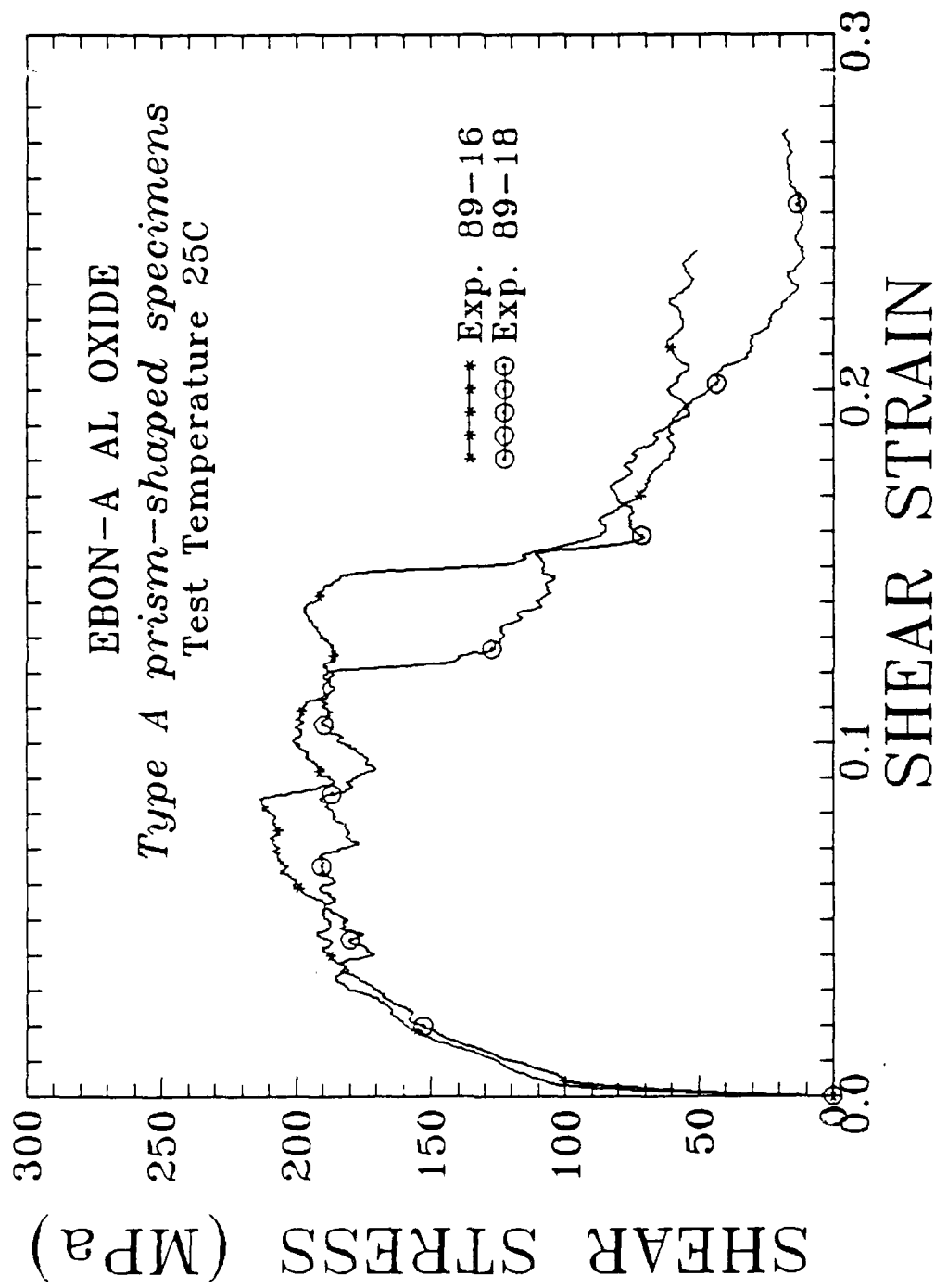


Fig. 2.10 Shear stress-strain diagrams for aluminum oxide from tests with prism-shaped specimens of type A. Prisms connected mechanically on one side and cemented on the other side.

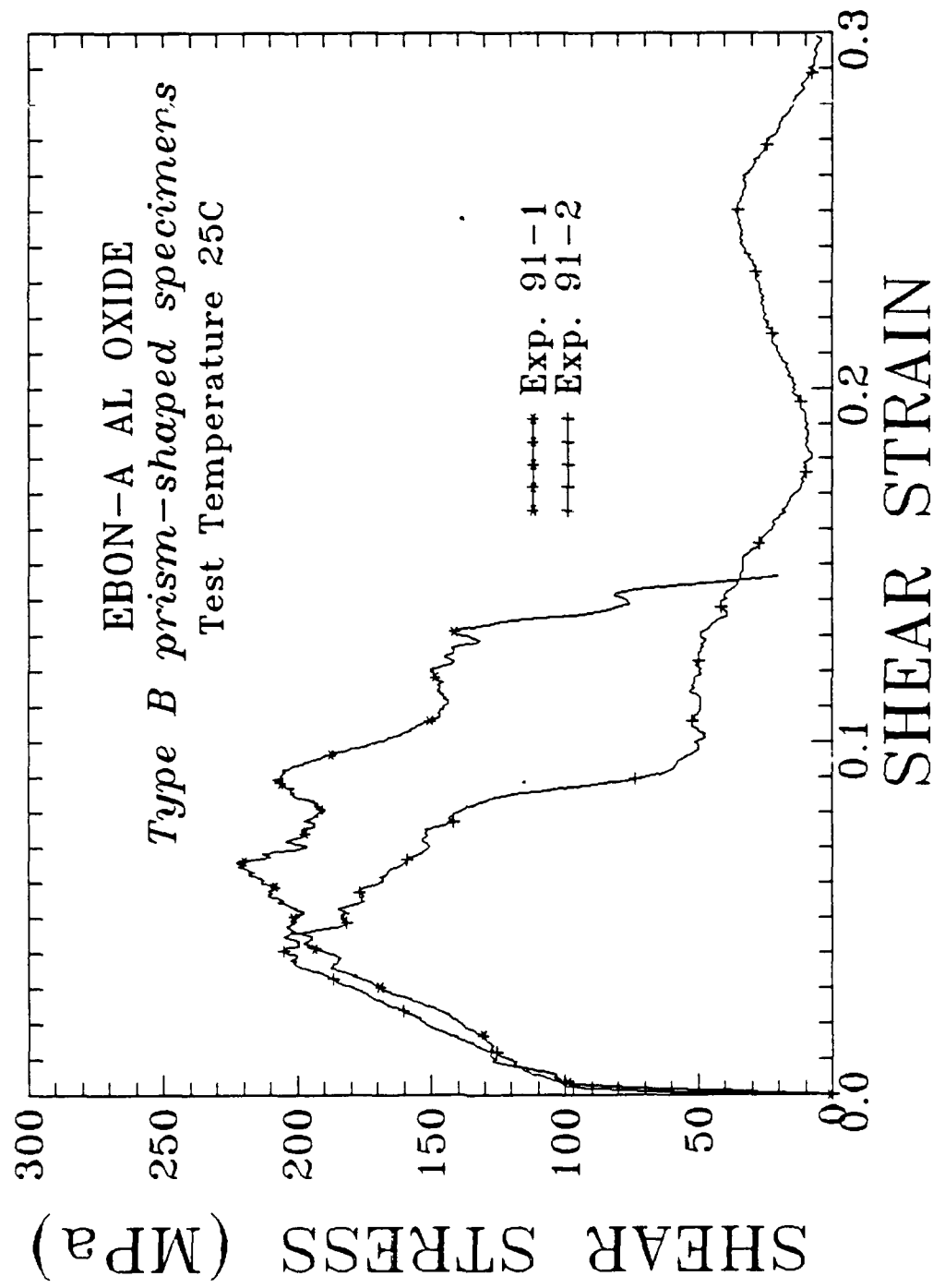


Fig. 2.11 Shear stress-strain diagrams for aluminum oxide from tests with prism-shaped specimens of type B. Prisms connected mechanically on one side and cemented on the other side.



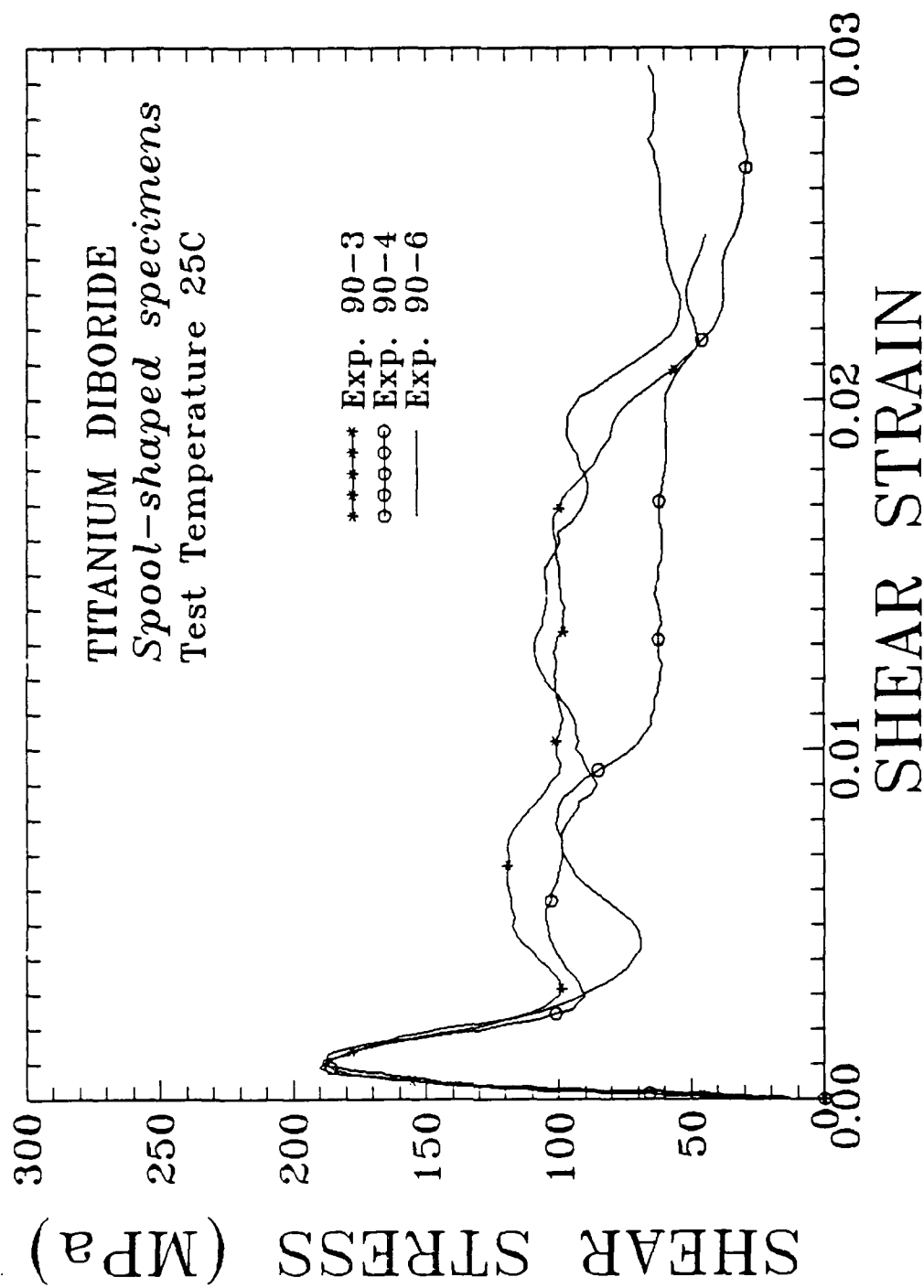


Fig. 2.12 Shear stress-strain diagram for titanium diboride.

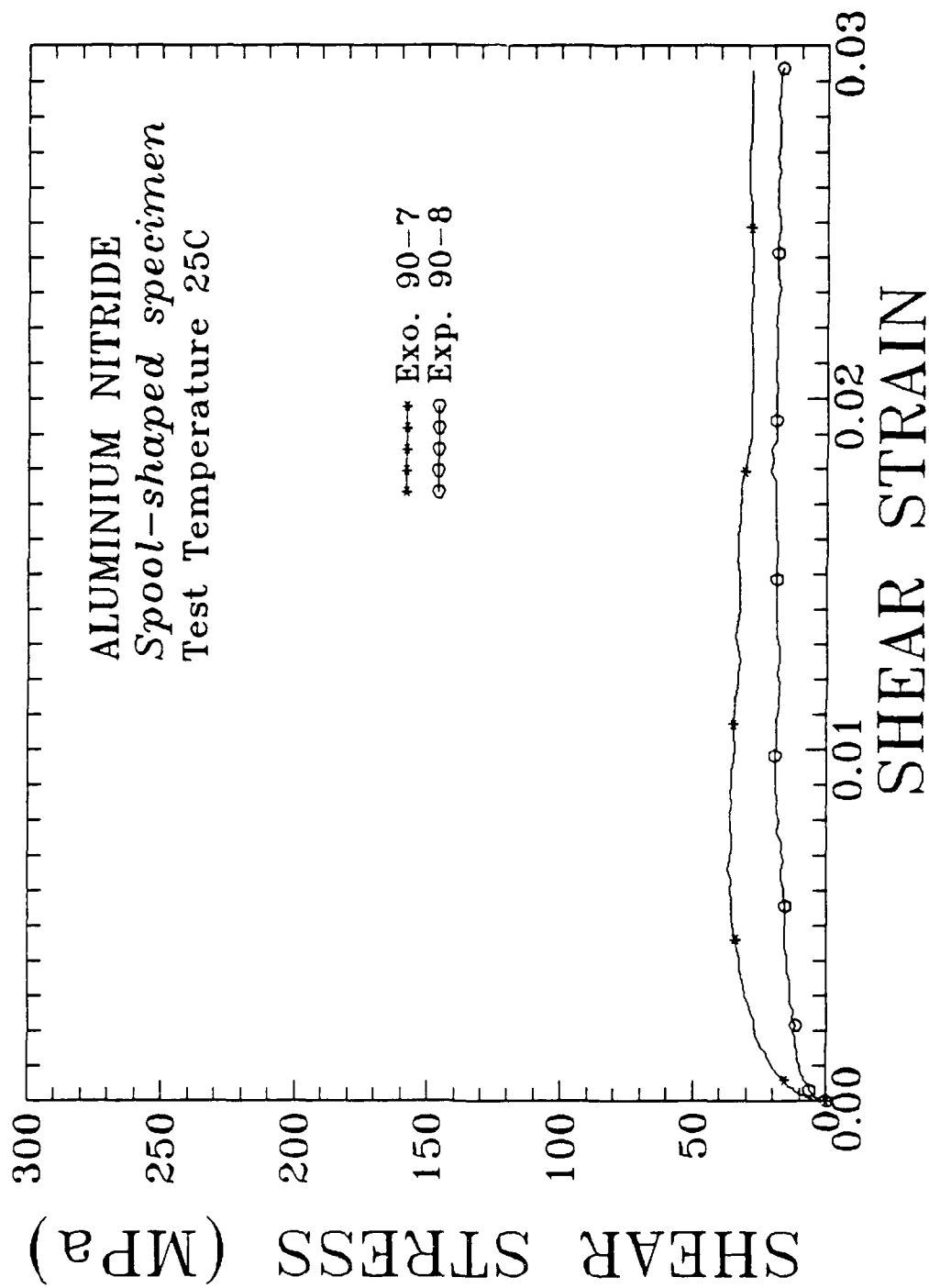


Fig. 2.13 Shear stress-strain diagram for aluminum nitride.

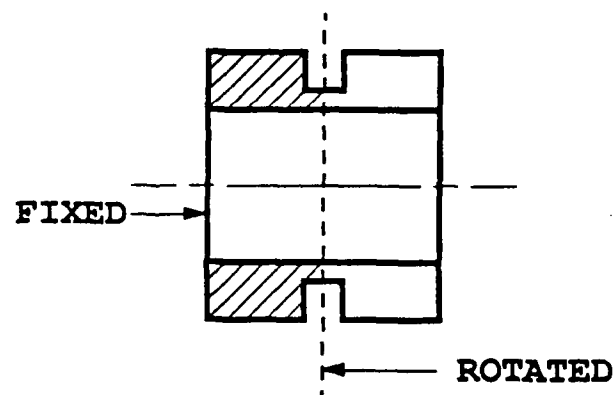


Fig. 3.1 Spool specimen geometry and boundary conditions for the finite element analysis.

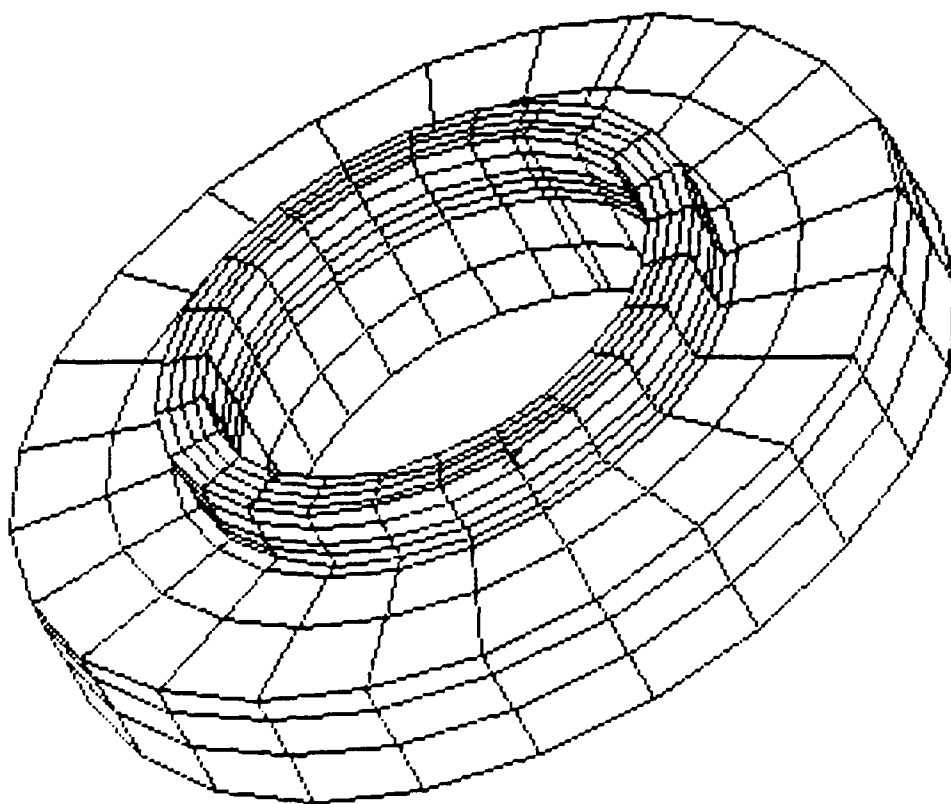


Fig. 3.2      Finite element discretization scheme for spool specimens.

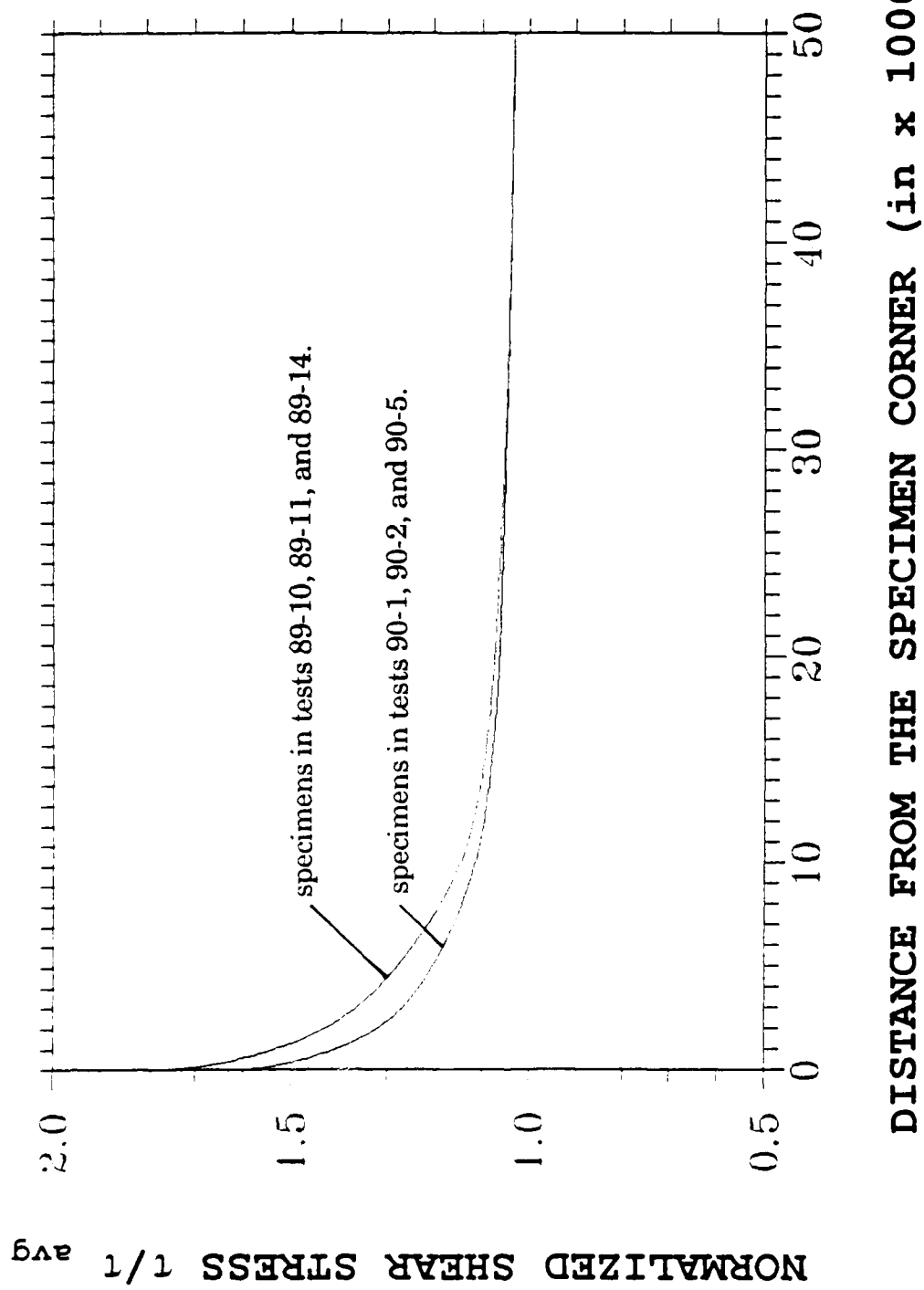


Fig. 3.3 Shear stress distribution along the specimen.

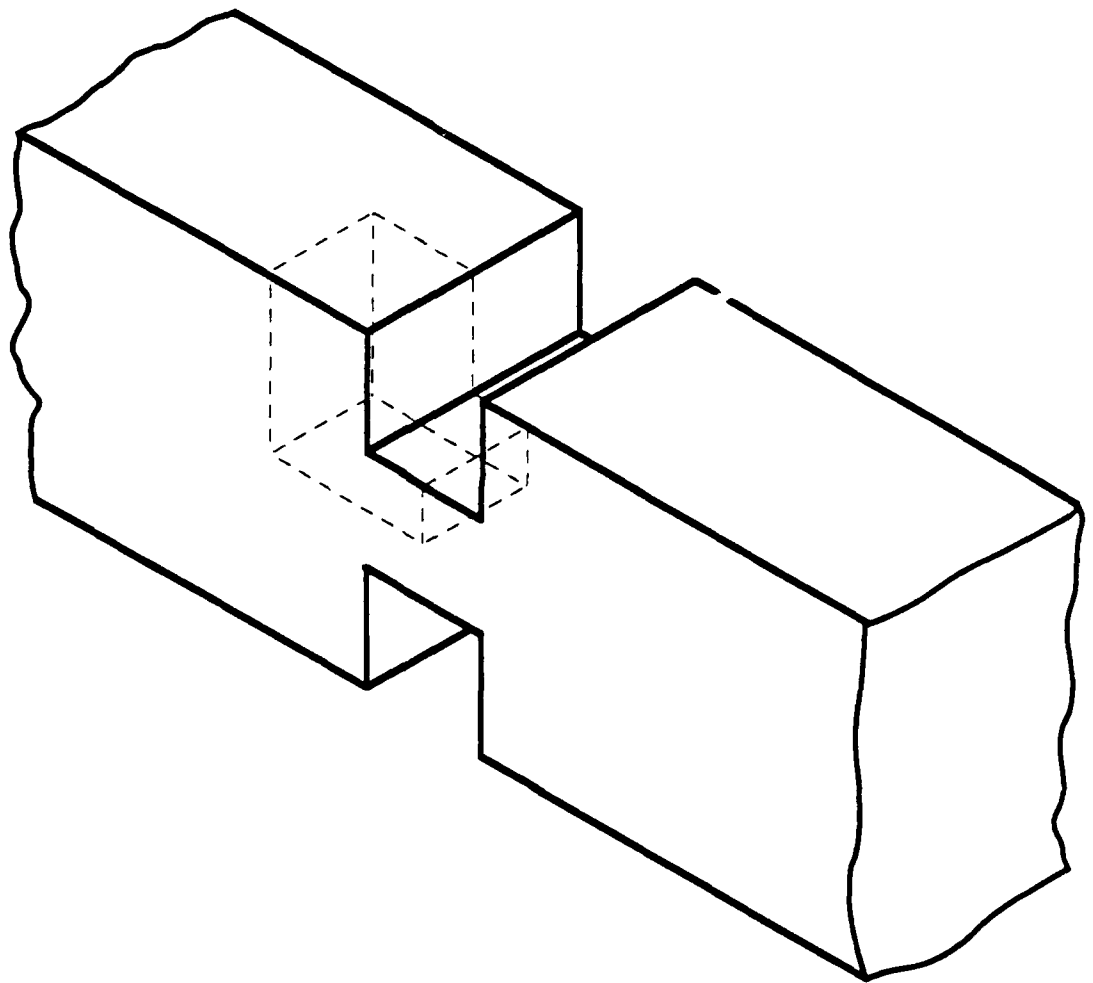


Fig. 3.4      Prism-shaped specimen modeled numerically (geometry A).

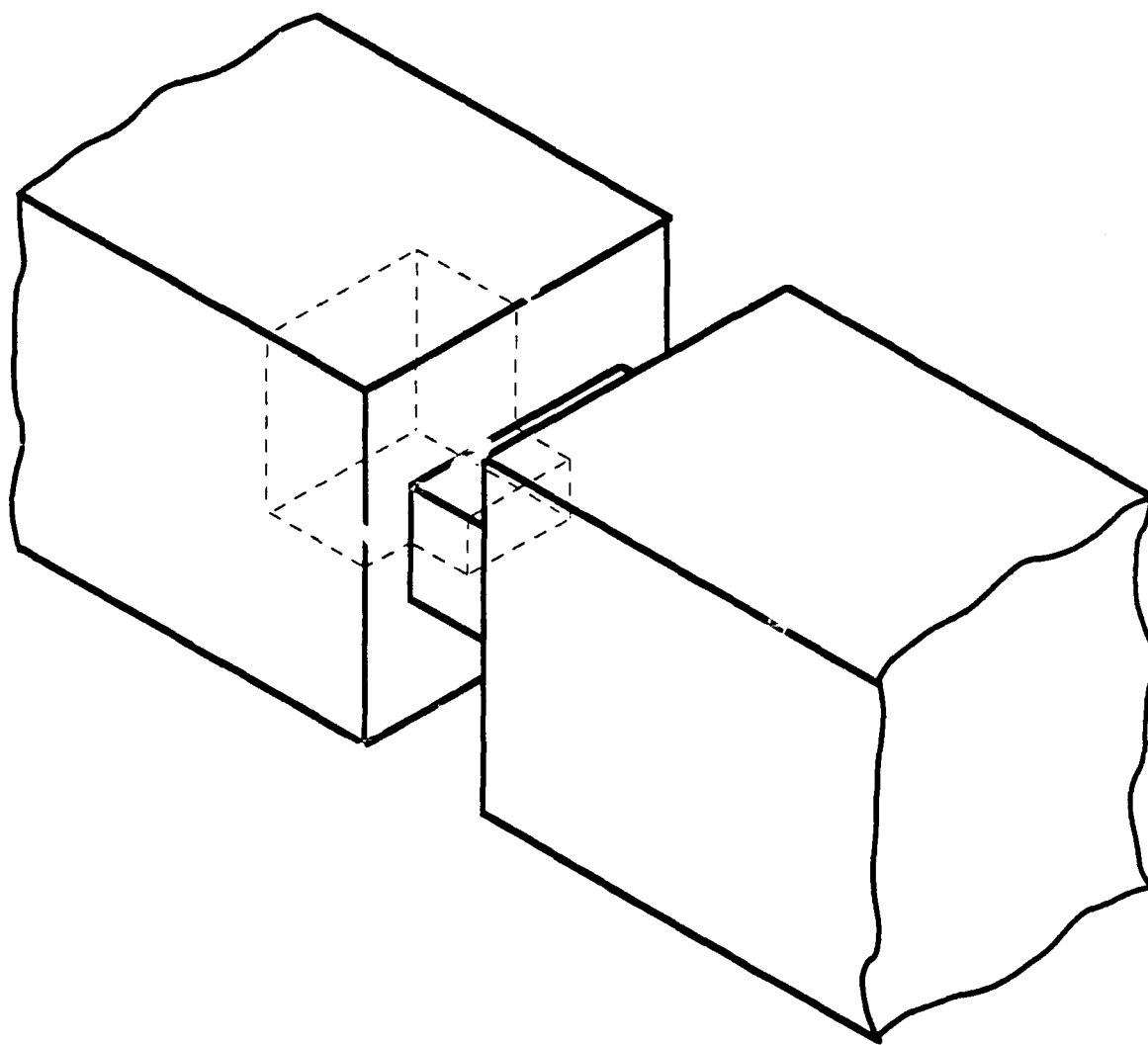


Fig. 3.5 Prism-shaped specimen modeled numerically (geometry B).

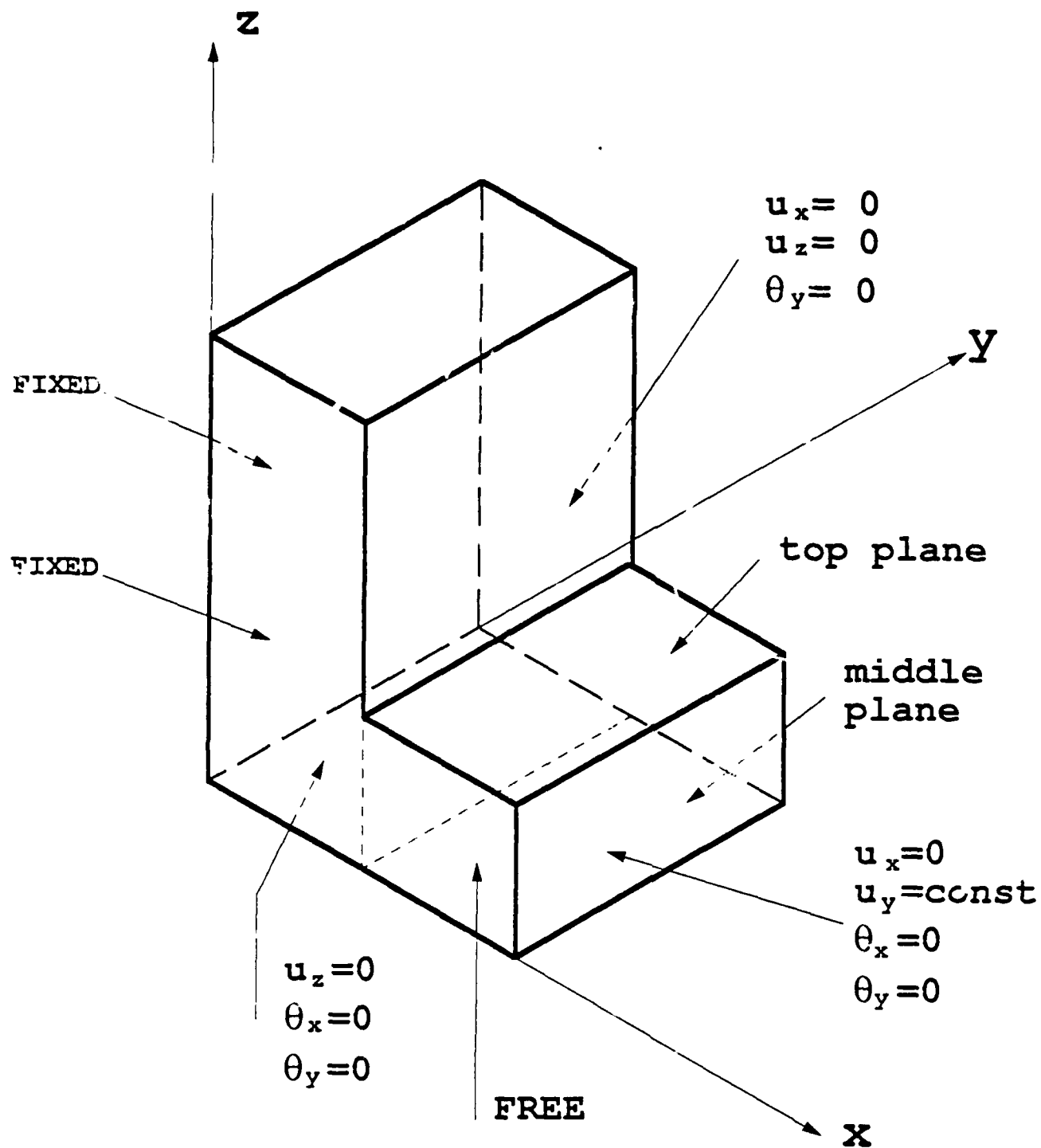


Fig. 3.6 Boundary conditions for the numerical analysis (prism A)



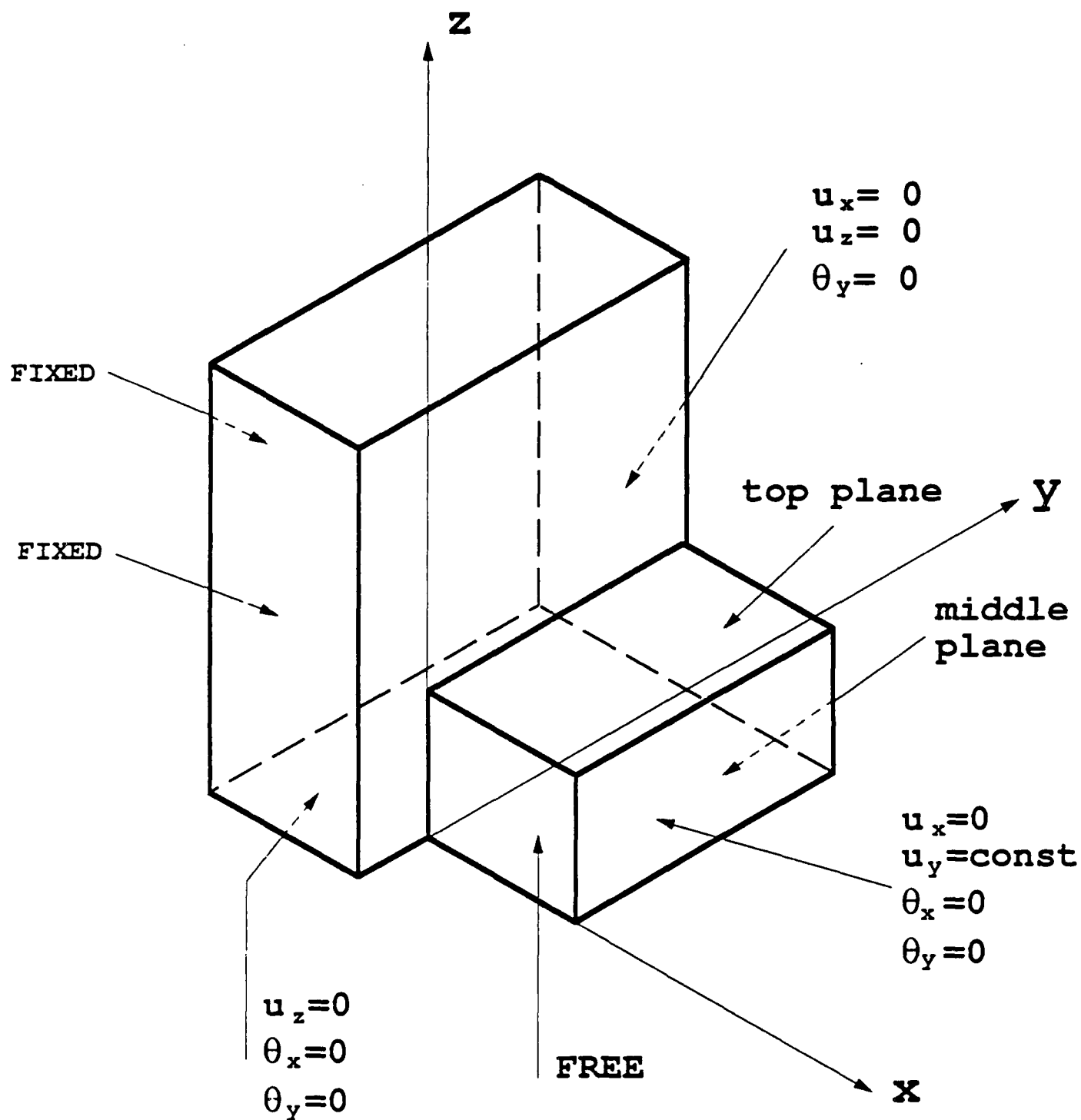


Fig. 3.7 Boundary conditions for the numerical analysis (prism B)

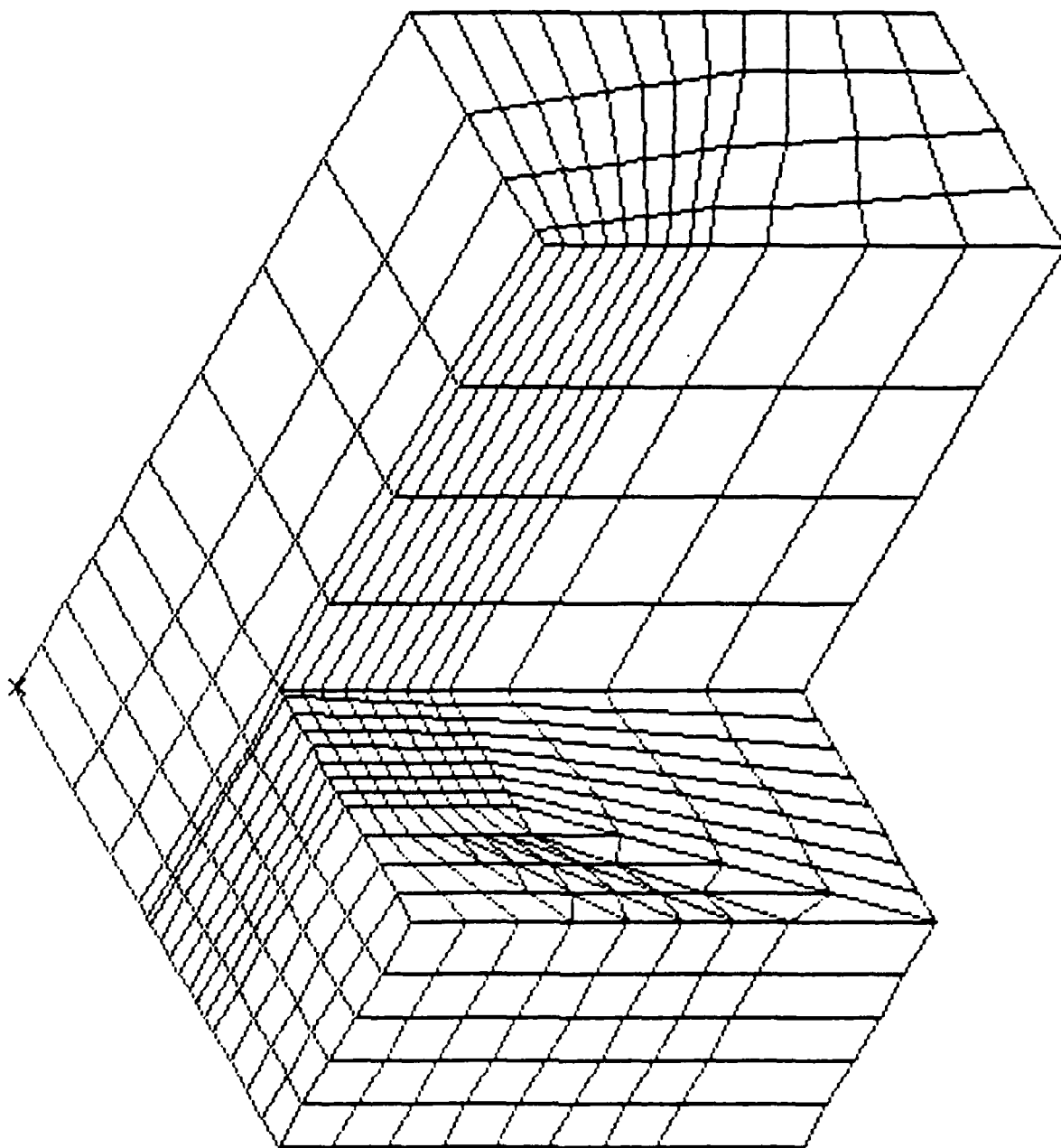


Fig. 3.8      Finite element discretization for prism-shaped specimens (geometry A)

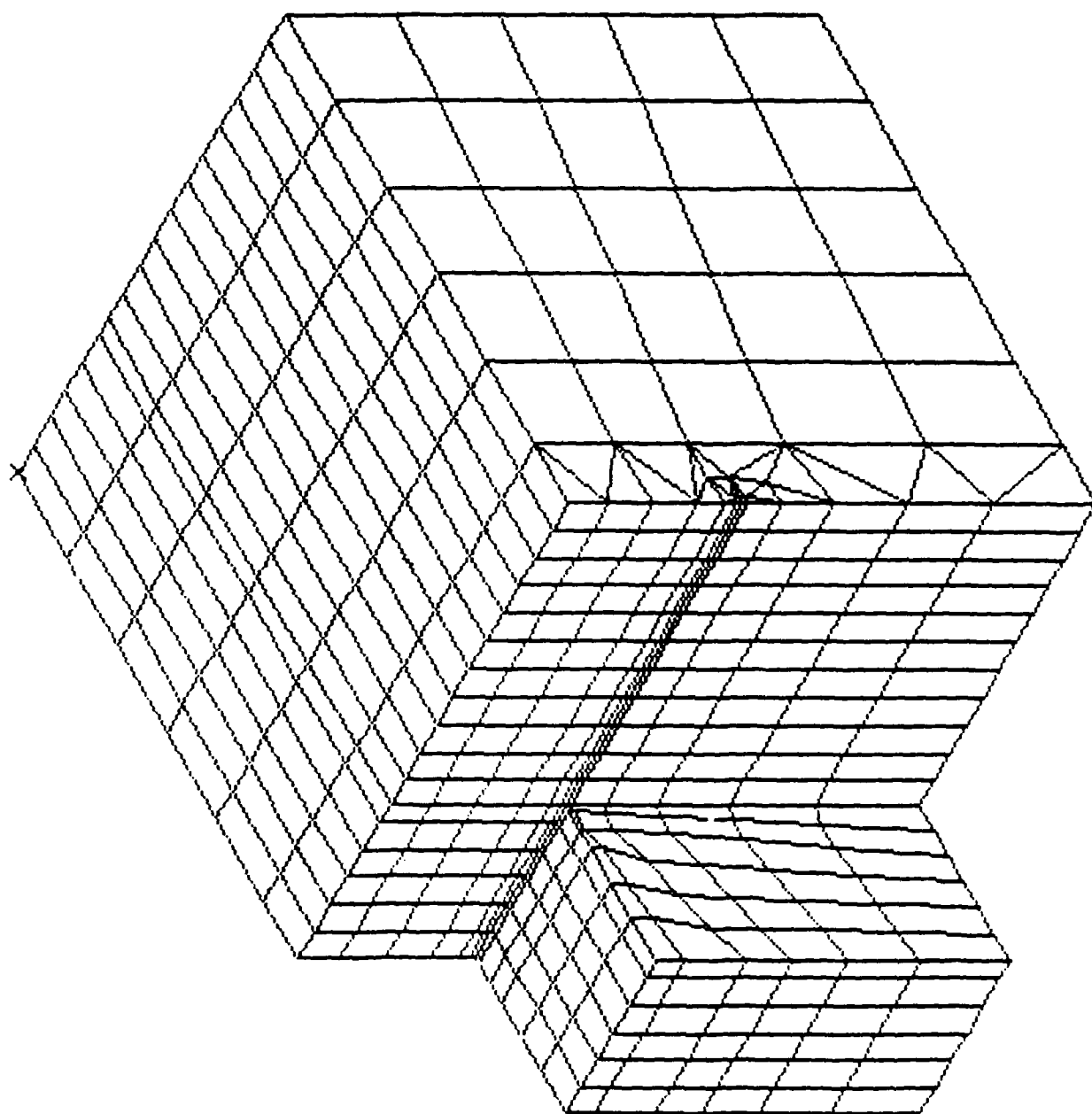


Fig. 3.9      Finite element discretization for prism-shaped specimens (geometry B).

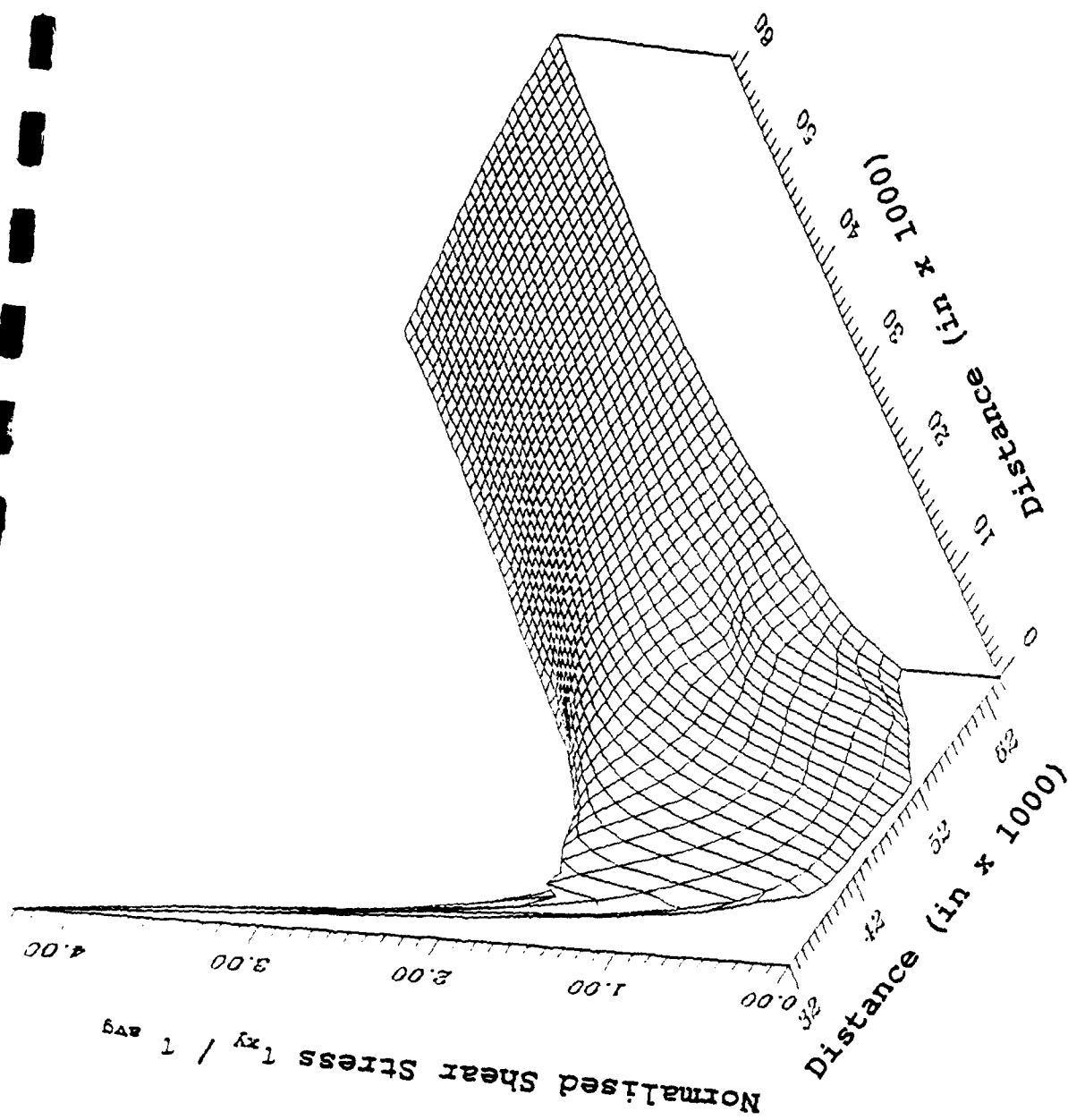


Fig. 3.10 Shear stress ( $\tau_{xy}$ ) distribution on the middle plane of prism specimens (geometry A)

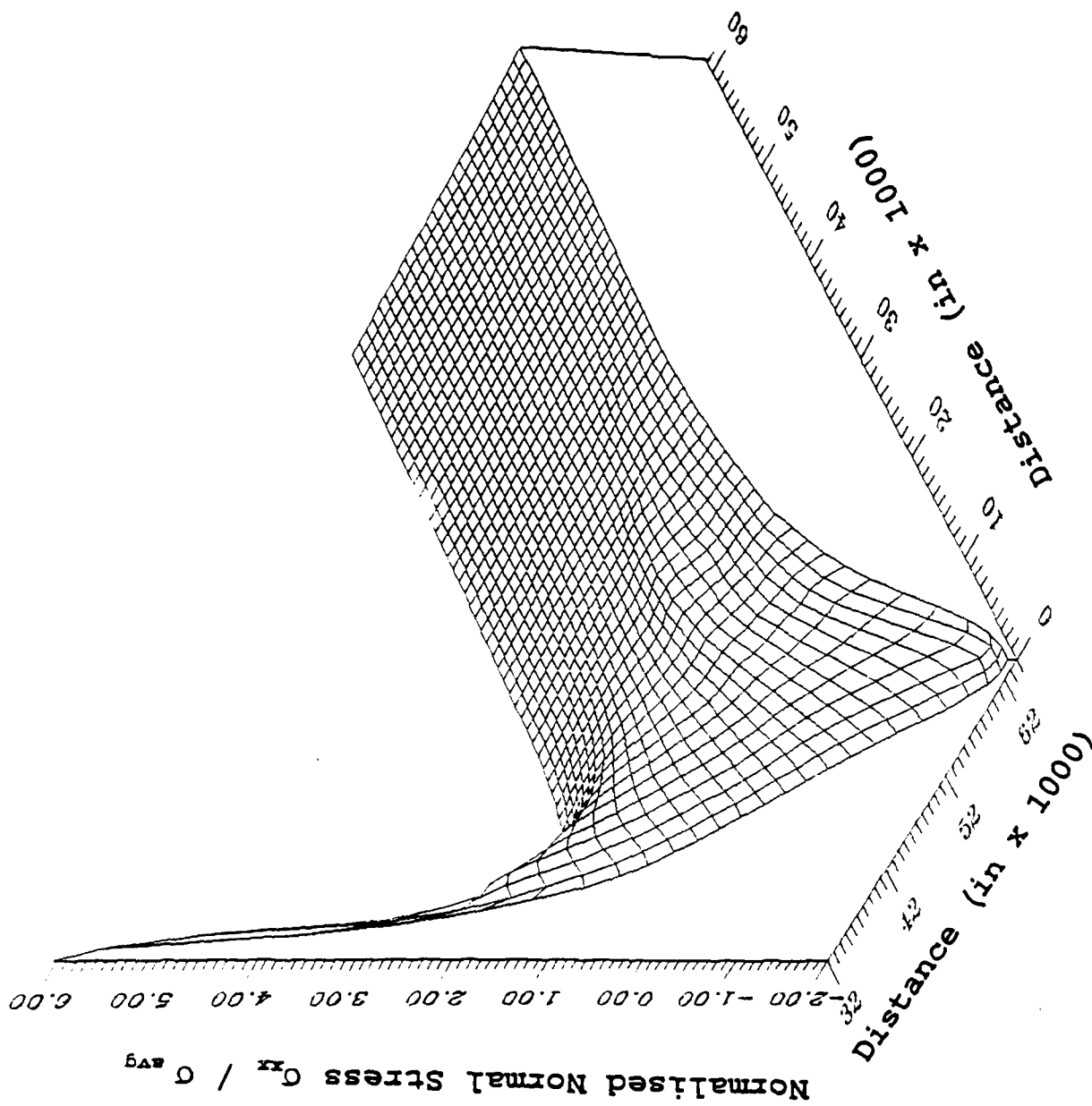


Fig. 3.11 Shear stress ( $\sigma_{xx}$ ) distribution on the middle plane of prism specimens (geometry A).

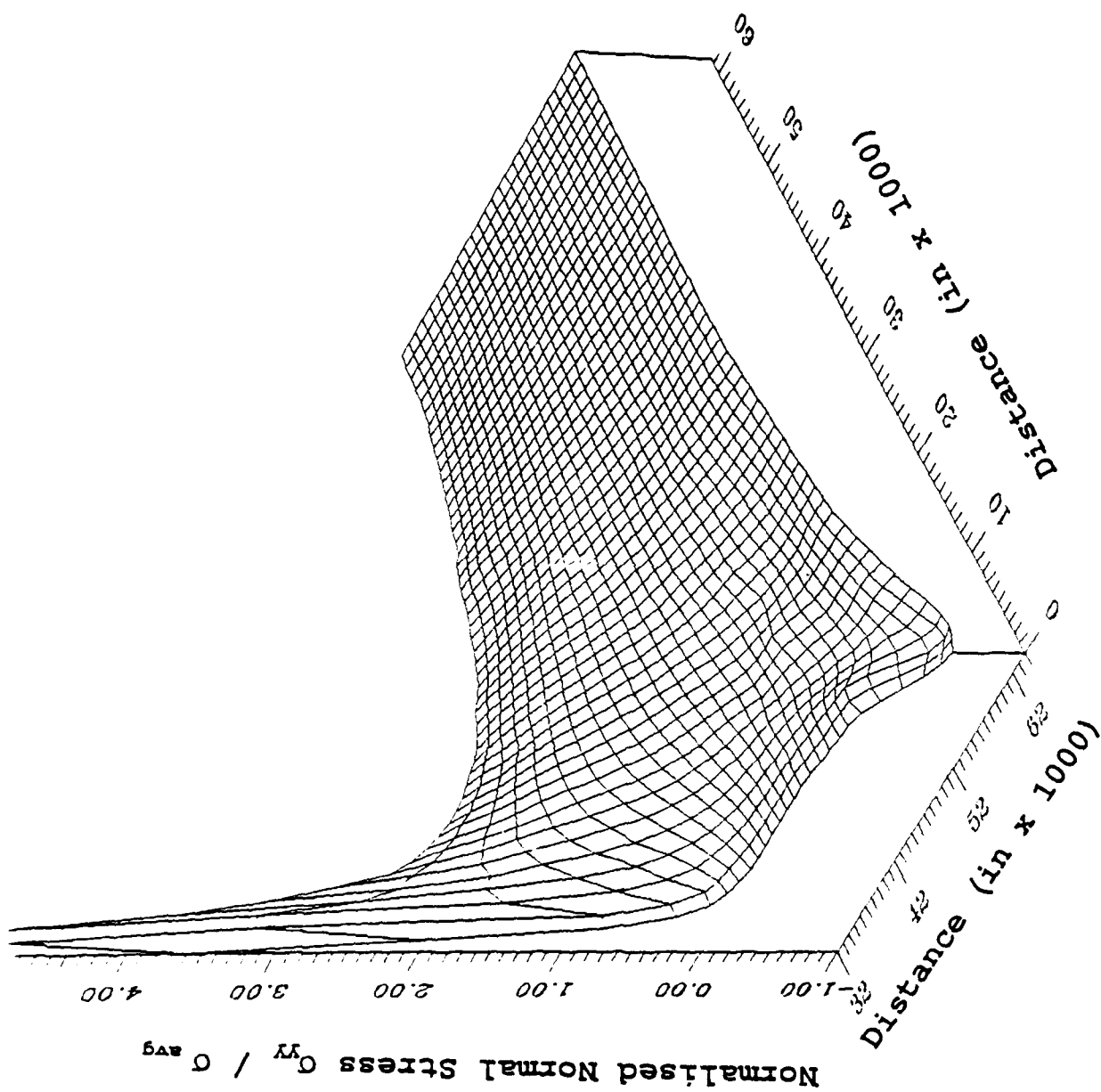


Fig. 3.12 Shear stress ( $\sigma_{yy}$ ) distribution on the middle plane of prism specimens (geometry A).

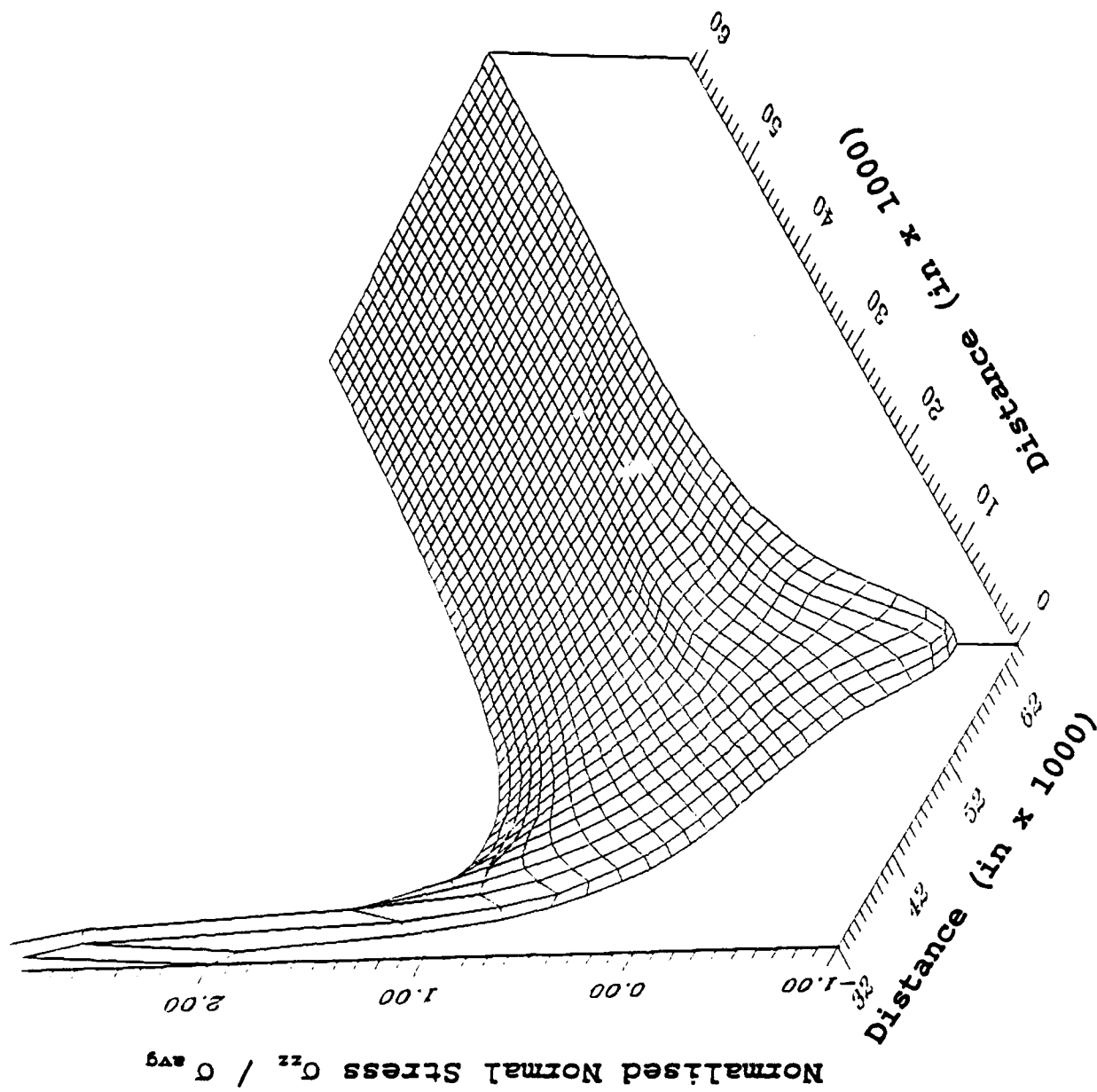


Fig. 3.13 Shear stress ( $\sigma_{zz}$ ) distribution on the middle plane of prism specimens (geometry A).

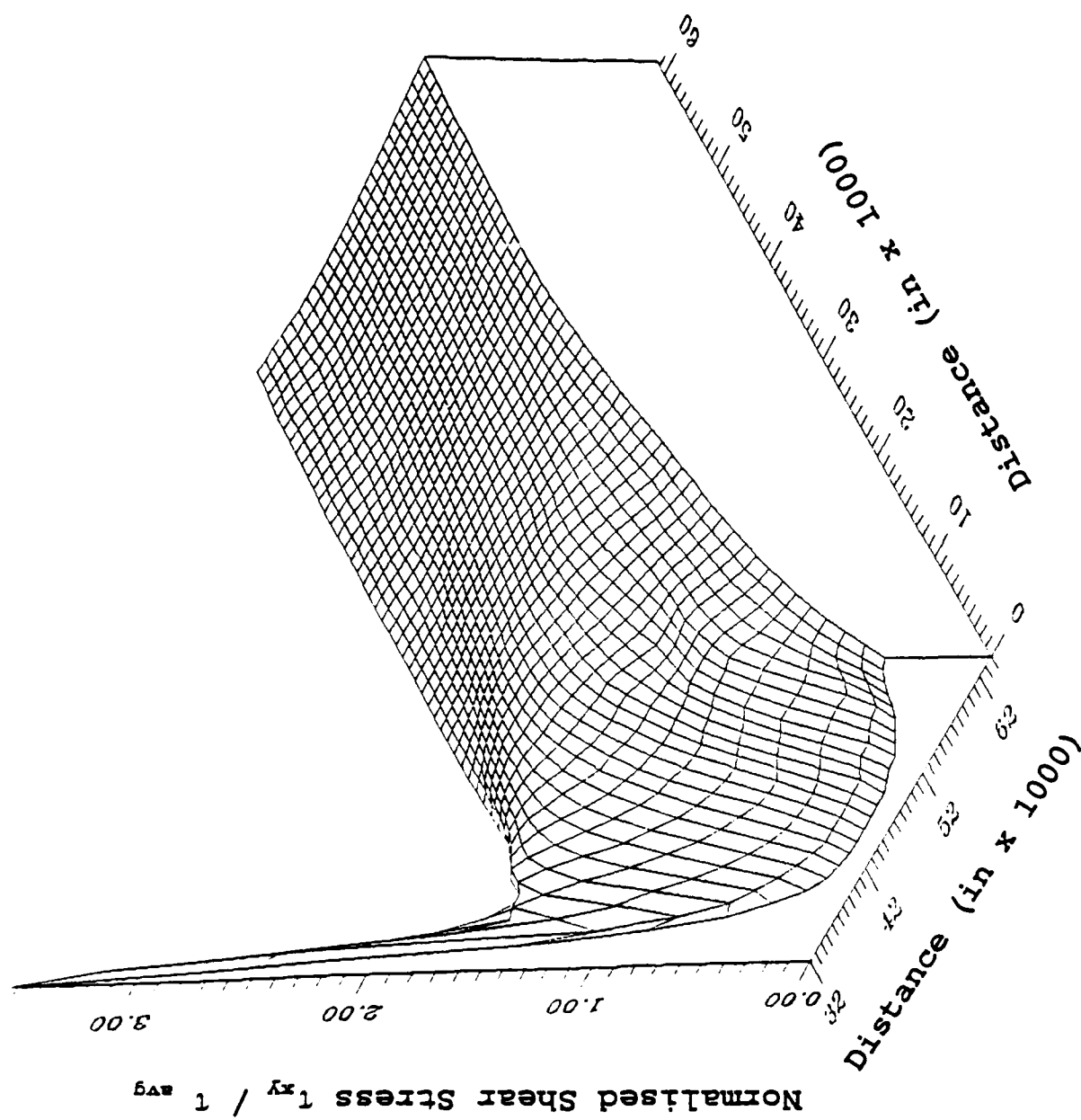


Fig. 3.14 Shear stress ( $\tau_{xy}$ ) distribution on the top plane of prism specimens (geometry A).



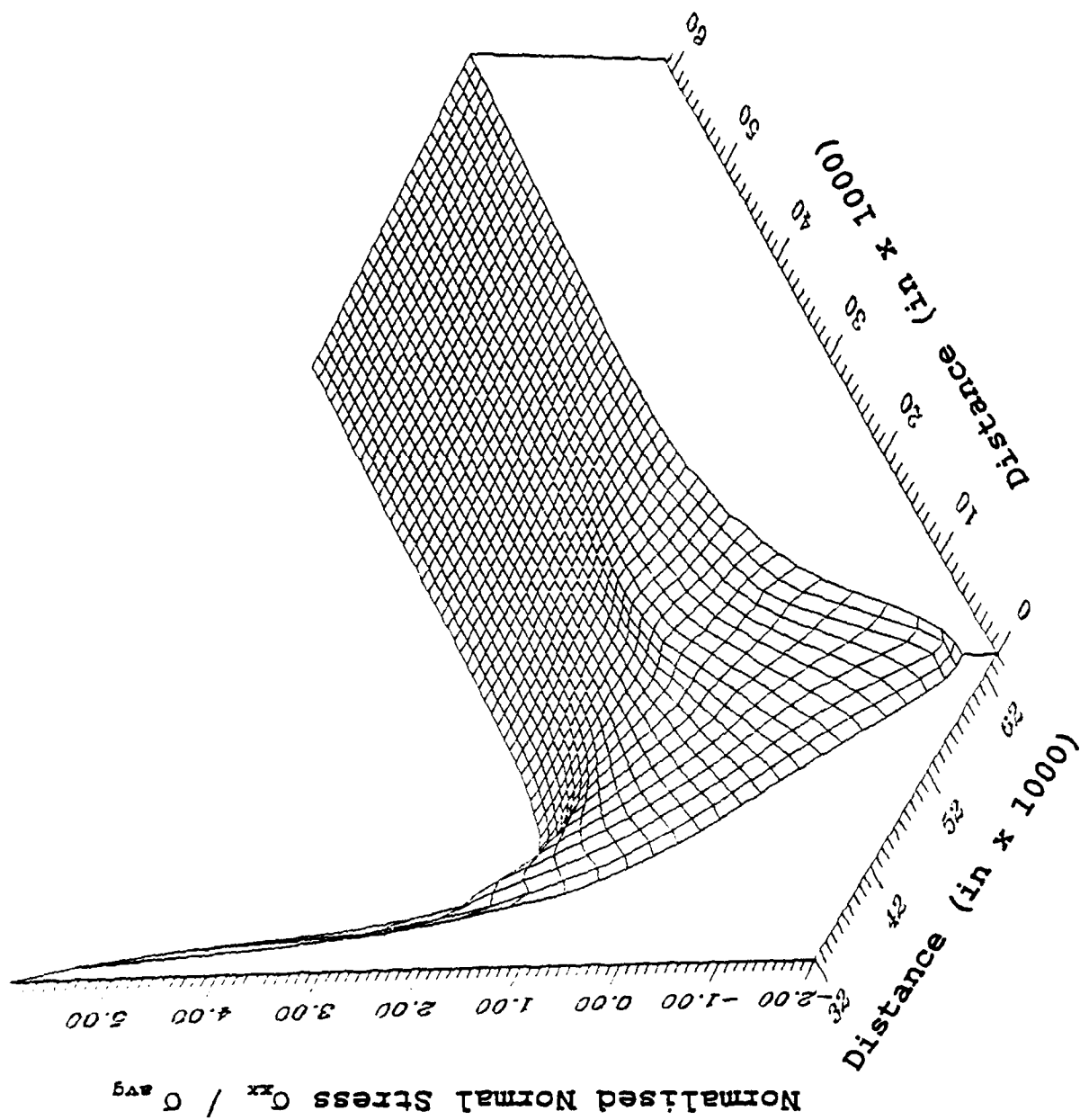


Fig. 3.15 Shear stress ( $\sigma_{xx}$ ) distribution on the top plane of prism specimens (geometry A)

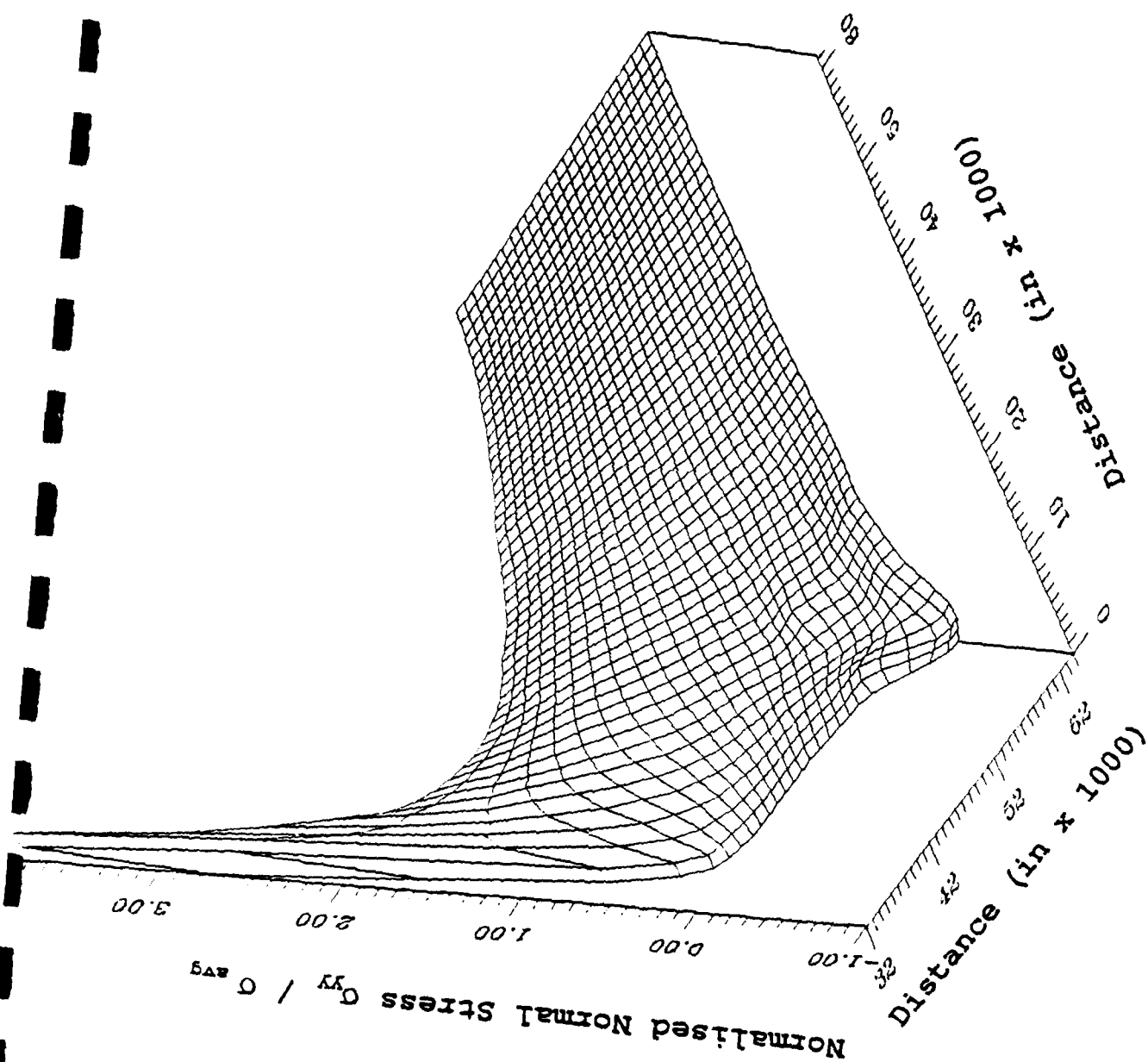


Fig. 3.16 Shear stress ( $\sigma_{yy}$ ) distribution on the top plane of prism specimens (geometry A)

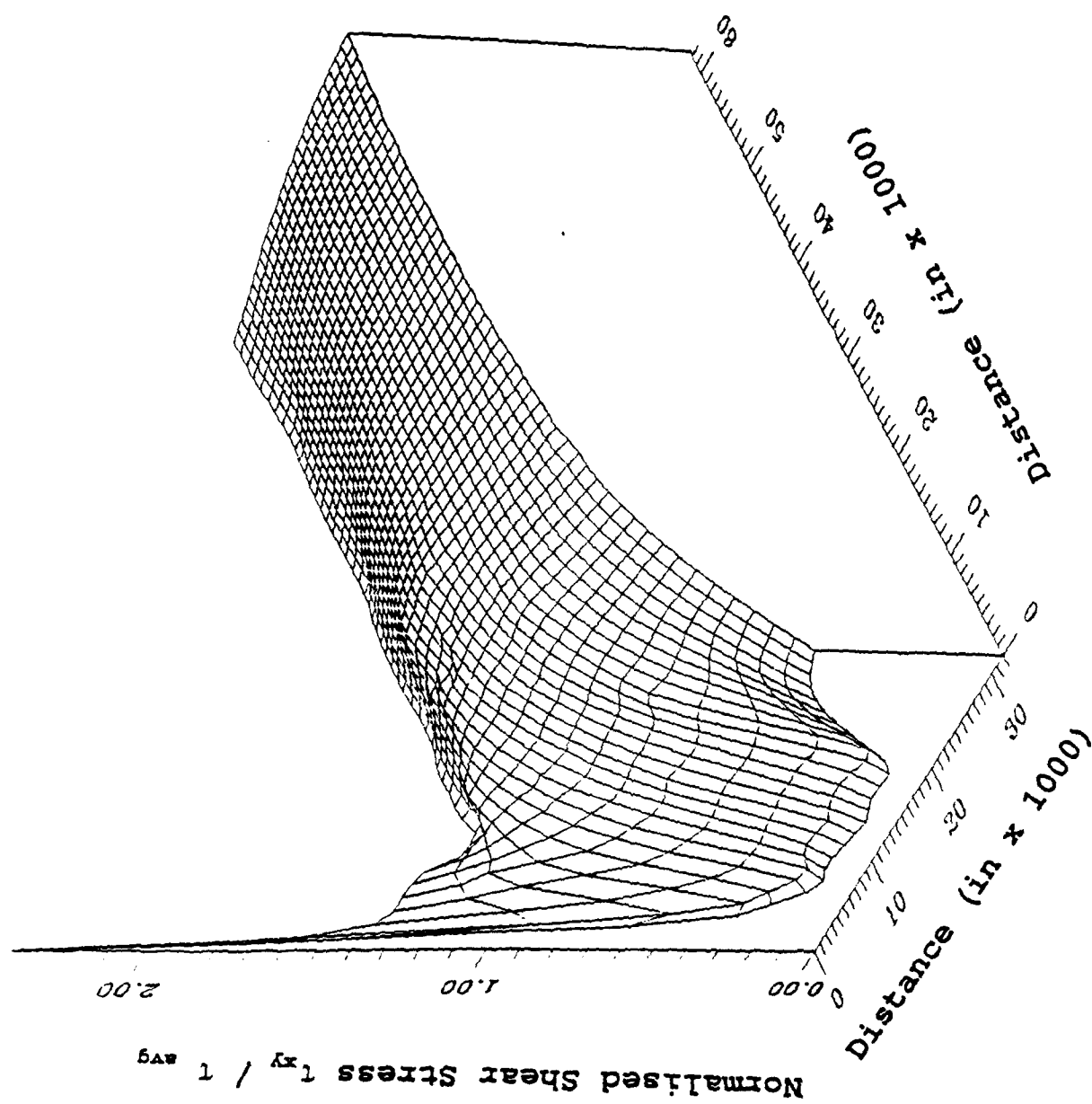


Fig. 3.17 Shear stress ( $\tau_{xy}$ ) distribution on the middle plane of prism specimens (geometry B)

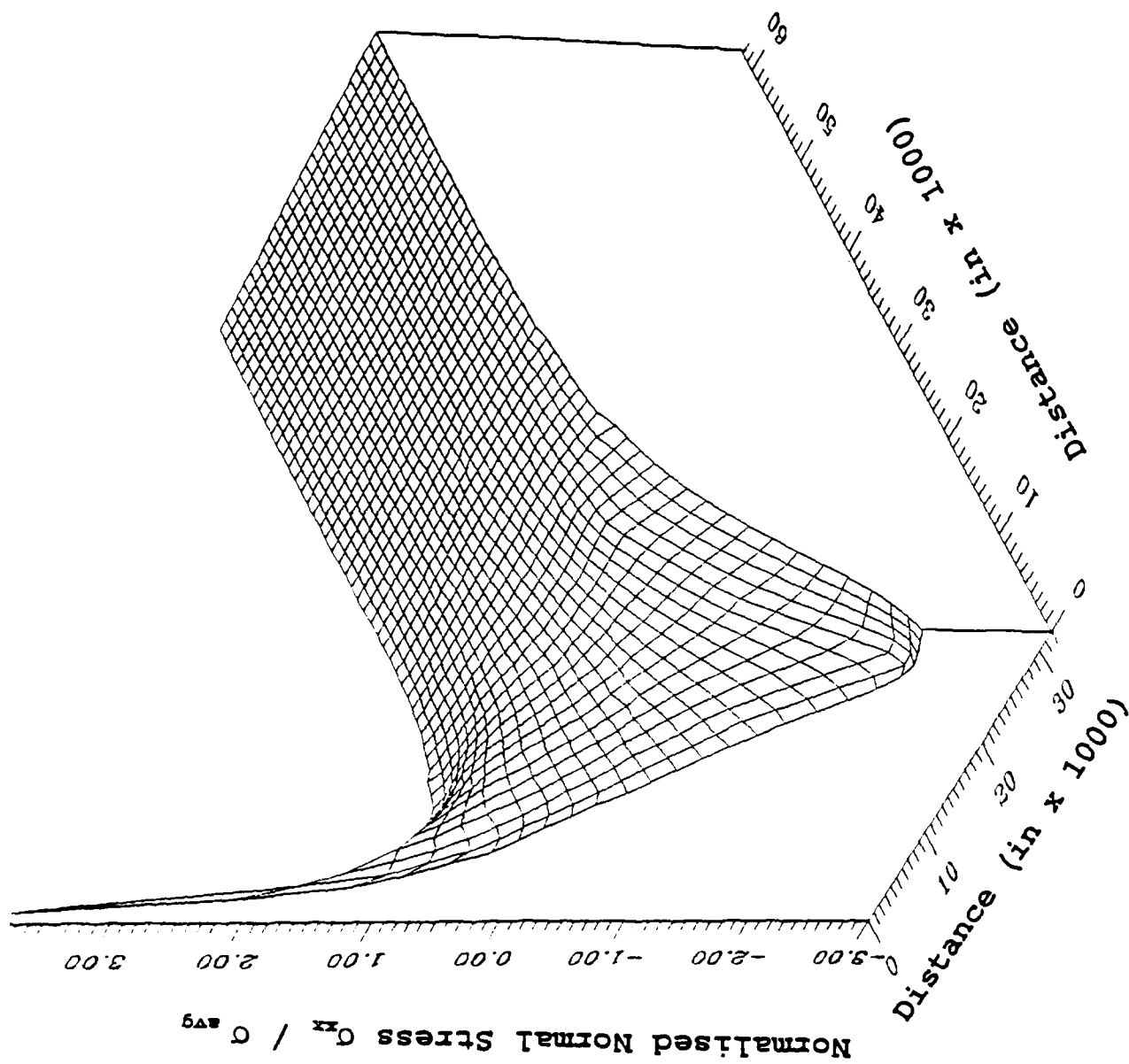


Fig. 3.18 Shear stress ( $\sigma_{xx}$ ) distribution on the middle plane of prism specimens (geometry B)

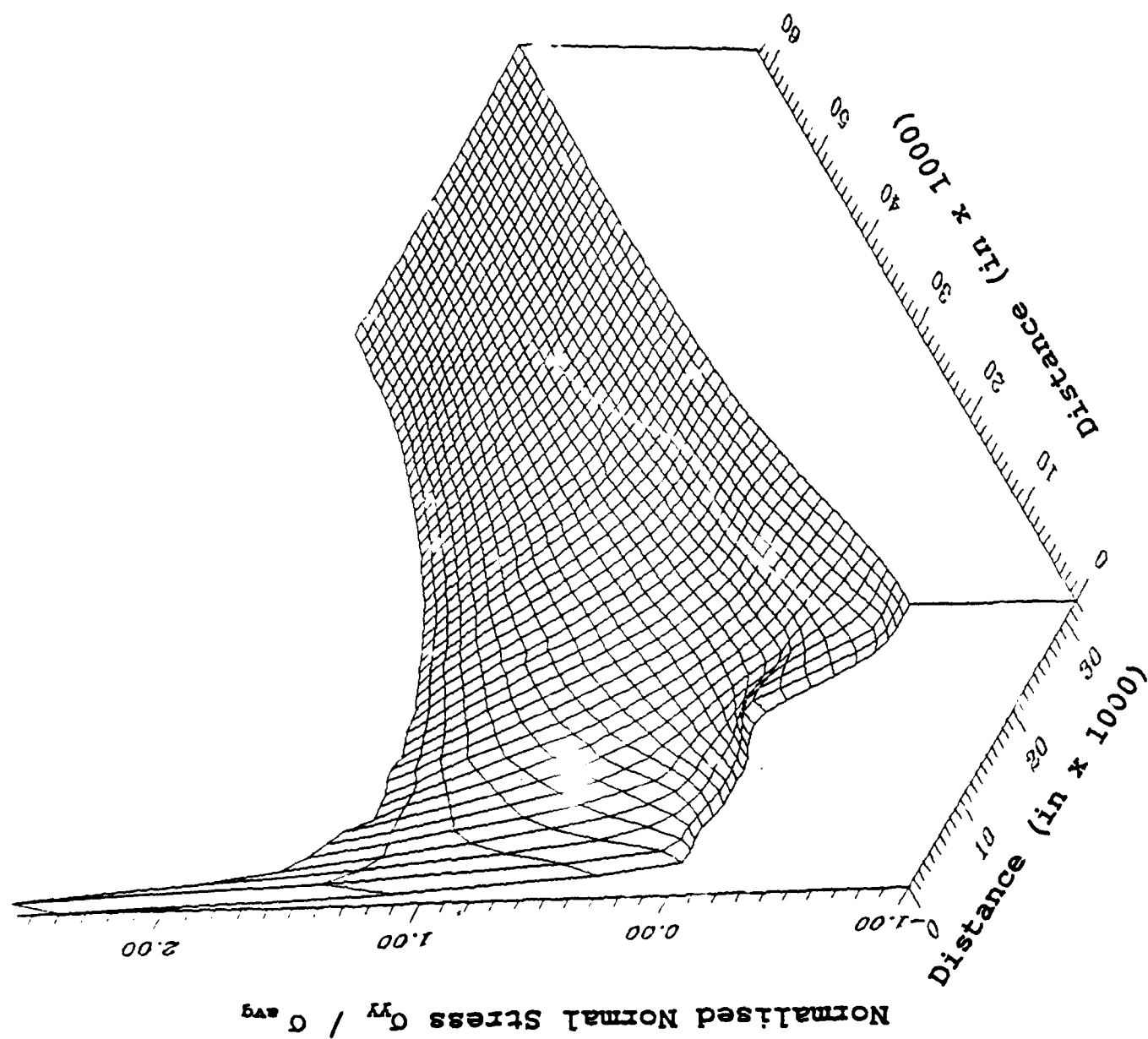


Fig. 3.19 Shear stress ( $\sigma_{xy}$ ) distribution on the middle plane of prism specimens (geometry B)

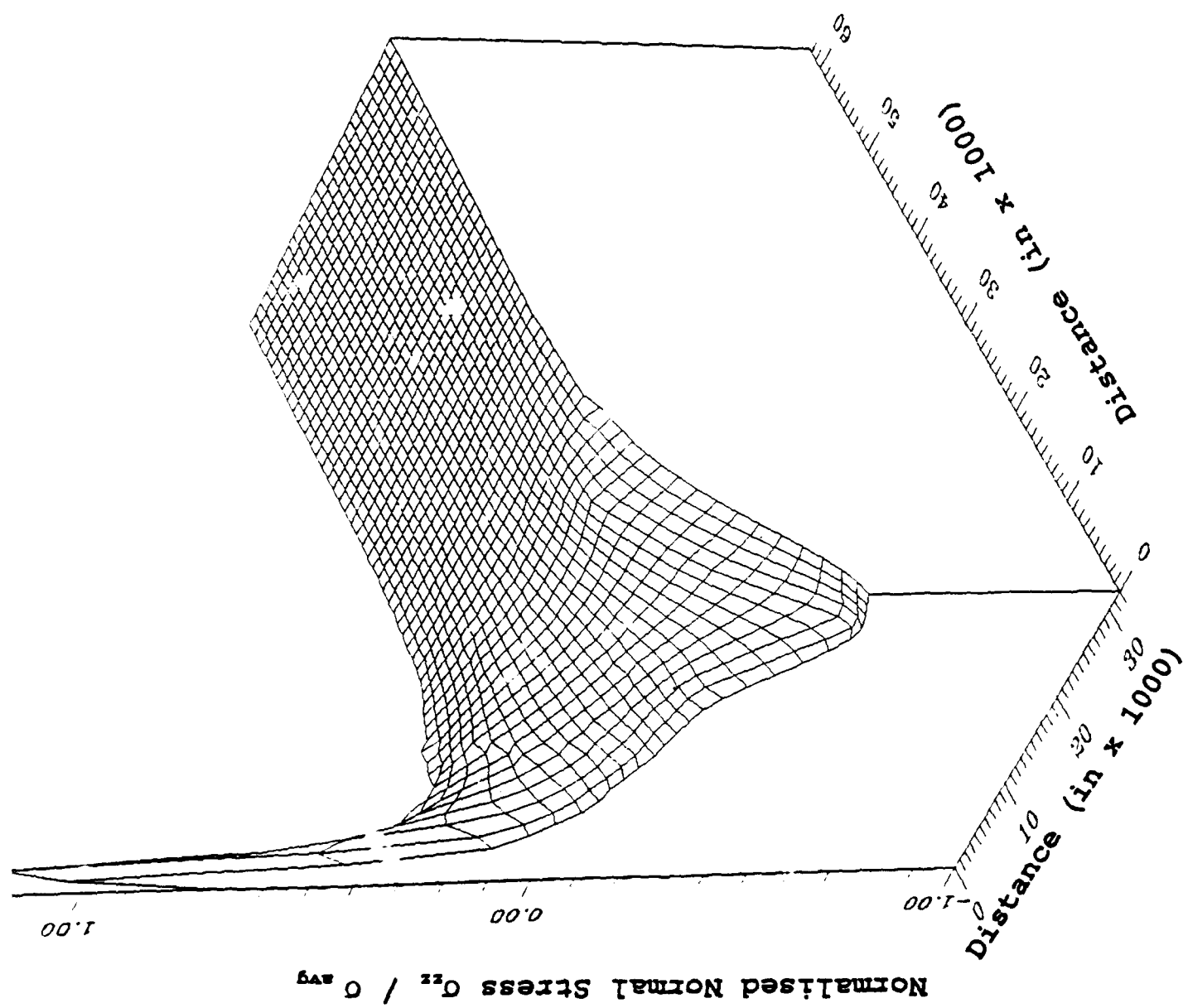


Fig. 3.20 Shear stress ( $\sigma_{zz}$ ) distribution on the middle plane of prism specimens (geometry B)

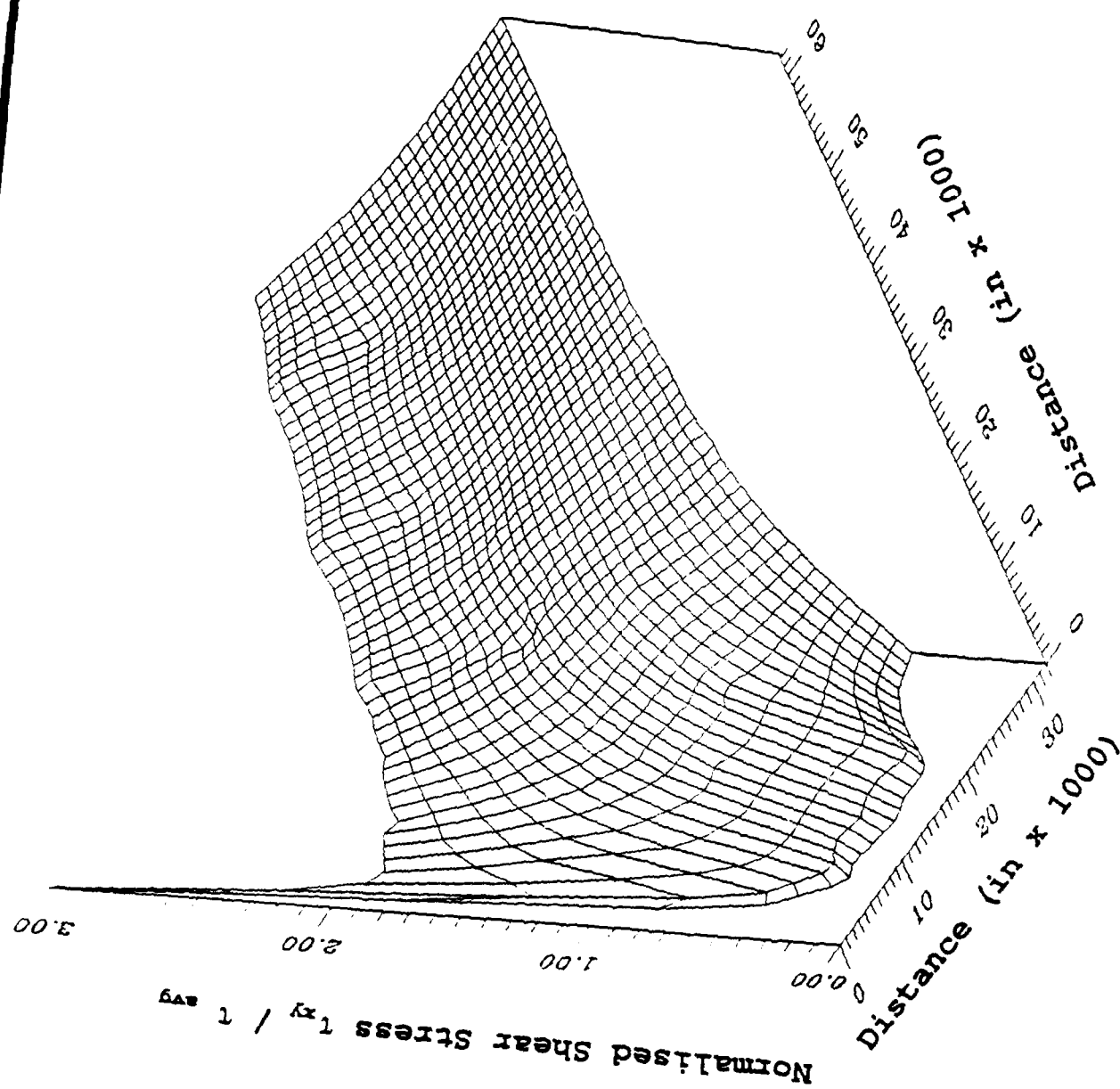


Fig. 3.21 Shear stress ( $\tau_{xy}$ ) distribution on the top plane of prism specimens (geometry B)

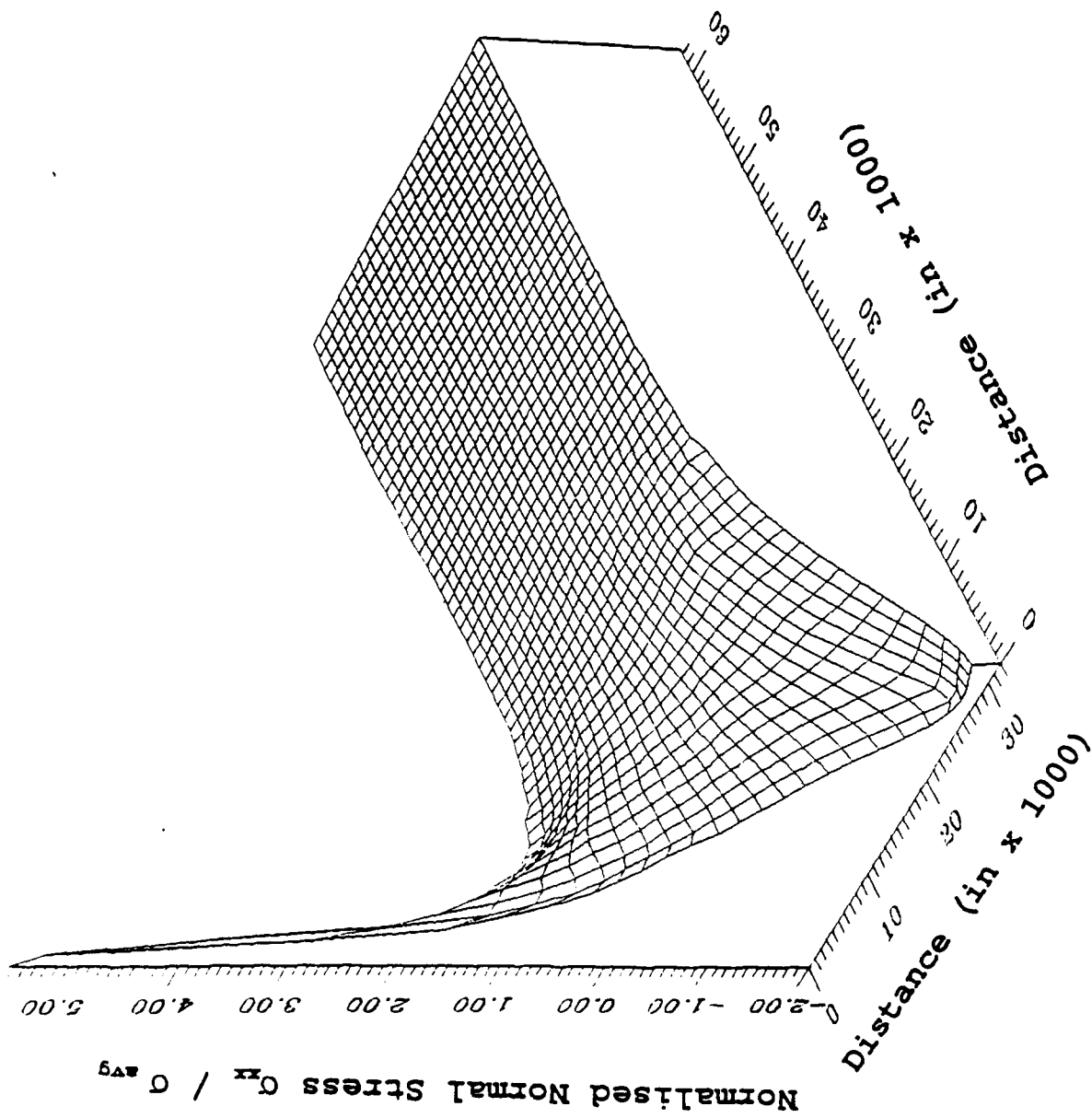


Fig. 3.22 Shear stress ( $\sigma_{xx}$ ) distribution on the top plane of prism specimens (geometry B)



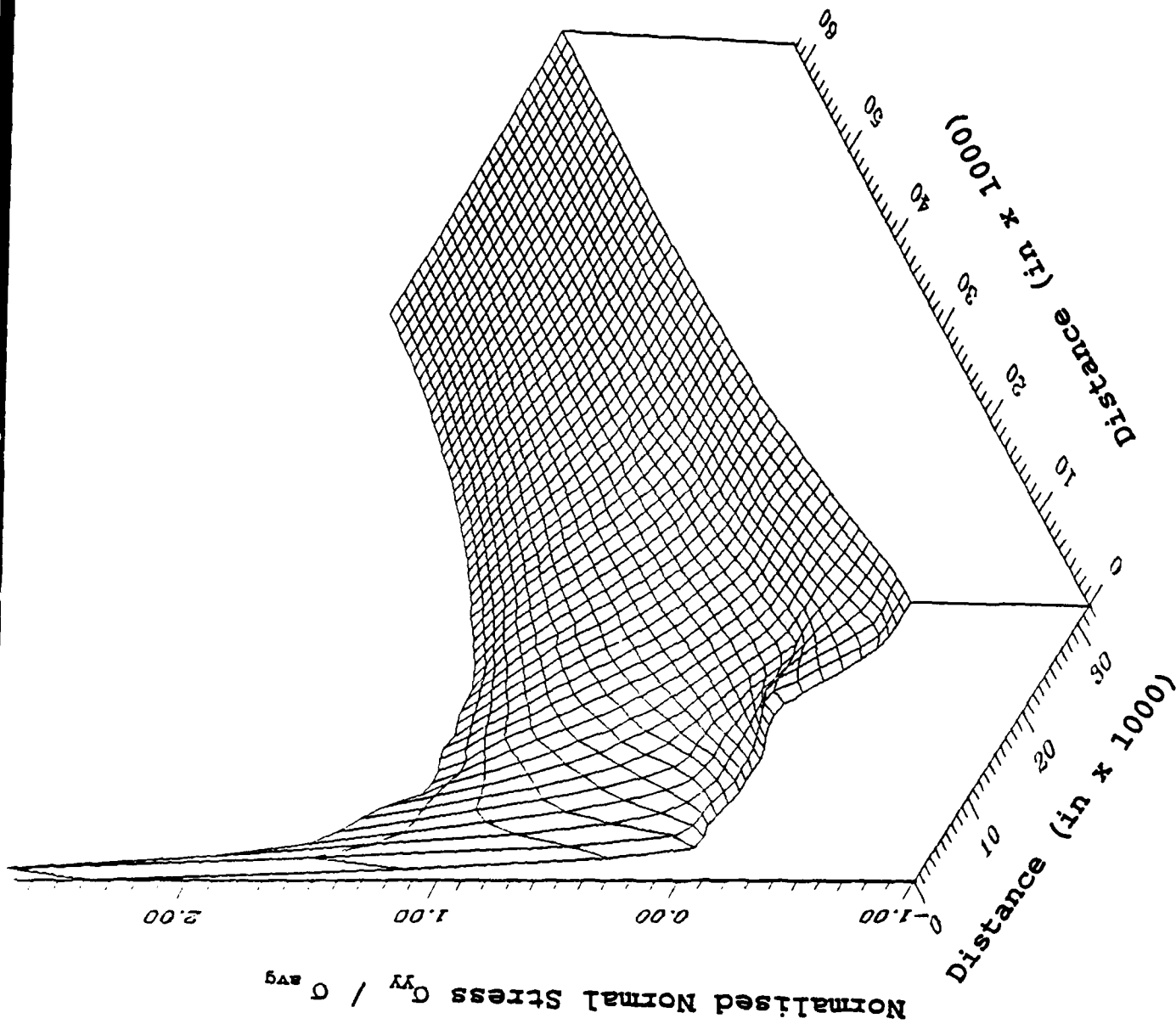


Fig. 3.23 Shear stress ( $\sigma_{yy}$ ) distribution on the top plane of prism specimens (geometry B)

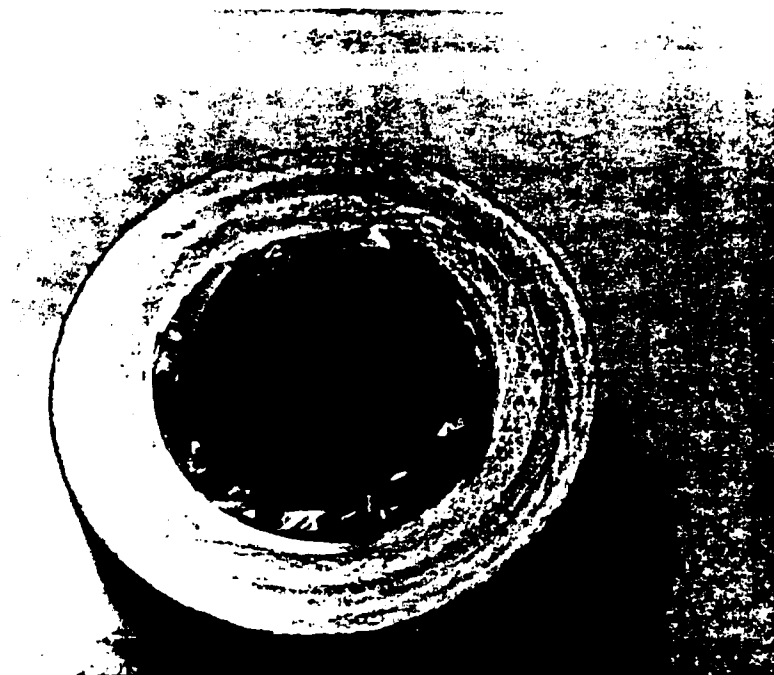


Fig. 4.1      Recovered spool-shaped aluminum oxide specimen.

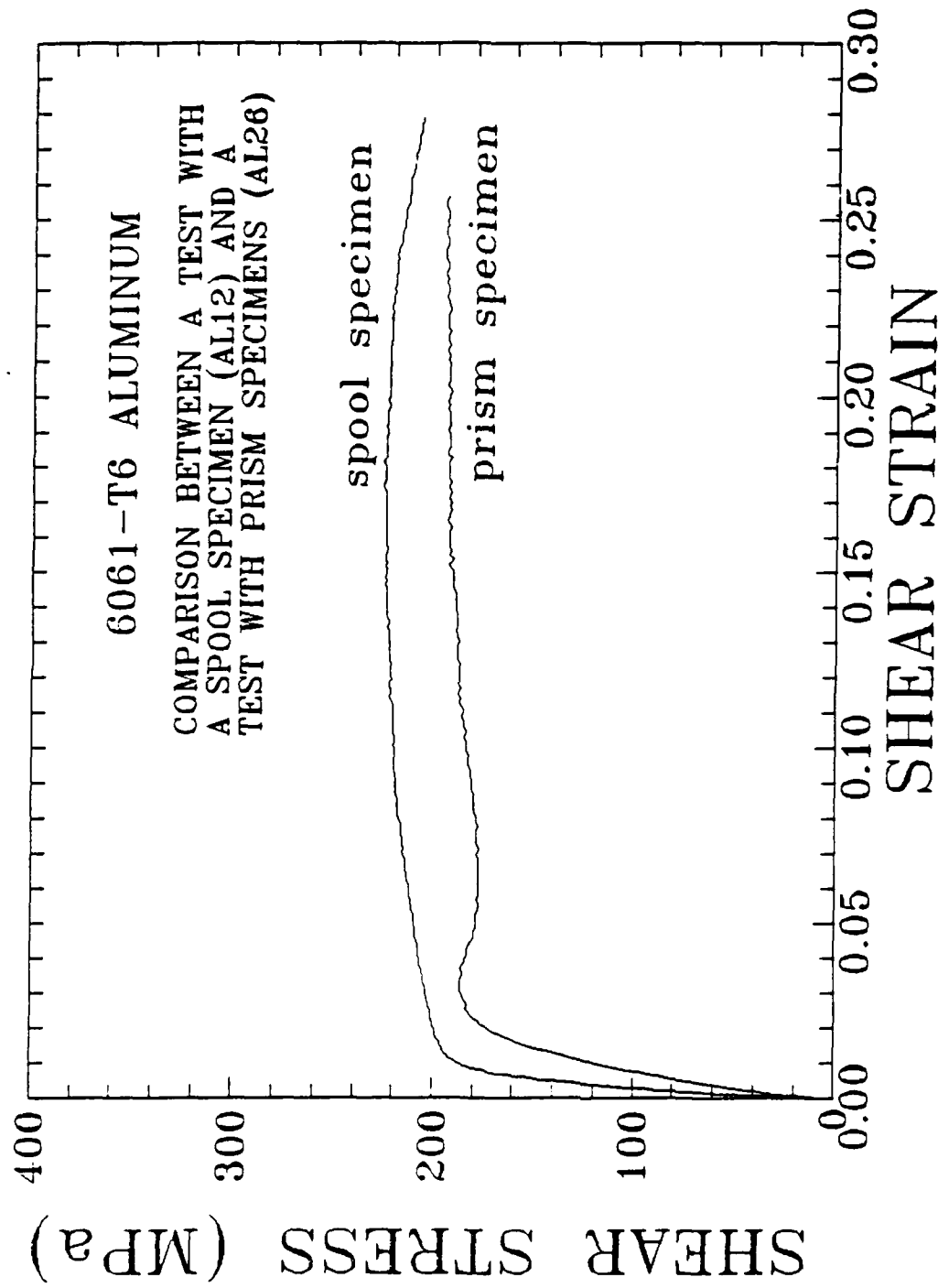


Fig. A.1 Shear stress-strain diagrams for 6061-T651 aluminum.